

Tidal Dissipation in Evolved Low and Intermediate Mass Stars

M. Esseldeurs¹, S. Mathis², and L. Decin¹

¹ Instituut voor Sterrenkunde, KU Leuven, Celestijnenlaan 200D, 3001 Leuven, Belgium
e-mail: mats.esseldeurs@kuleuven.be

² Université Paris-Saclay, Université Paris Cité, CEA, CNRS, AIM, 91191 Gif-sur-Yvette, France

Received; accepted

ABSTRACT

Context. As the observed occurrence for planets or stellar companions orbiting low and intermediate-mass evolved stars is increasing, so does the importance of understanding and evaluating the strength of their interactions. This is important for both the further evolution of our own Earth-Sun system, as well as most of the observed exoplanetary systems. One of the most fundamental mechanisms to understand this interaction is the tidal dissipation in these stars, as it is one of the engines of orbital/rotational evolution of star-planet/star-star systems.

Aims. This article builds on previous works studying the evolution of the tidal dissipation along the pre-main-sequence and the main-sequence of low-mass and intermediate-mass stars, which have shown the strong link between the structural and rotational evolution of stars and tidal dissipation. This article provides for the first time a complete picture of tidal dissipation along the entire evolution of low and intermediate-mass stars, including the advanced phases of evolution.

Methods. Using stellar evolutionary models, the internal structure of the star is computed from the pre-main sequence all the way up to the white dwarf phase, and this for stars with initial mass between 1 and $4 M_{\odot}$. Using this internal structure, the tidal dissipation is computed along the entire stellar evolution. Tidal dissipation is separated into two components: the dissipation of the equilibrium (non-wavelike) tide and the dissipation of the dynamical (wavelike) tide. For evolved stars the dynamical tide is constituted by progressive internal gravity waves. The evolution of the tidal dissipation is investigated and compared for both the equilibrium and dynamical tides.

Results. The significance of both the equilibrium and dynamical tide dissipation becomes apparent within distinct domains of the parameter space. The dissipation of the equilibrium tide is dominant when the star is large in size or the companion is far away from the star. Conversely the dissipation of the dynamical tide is important when the star is small in size or the companion is close to the star. The size and location of these domains depend on the masses of both the star and the companion, as well as the evolutionary phase.

Conclusions. Both the equilibrium and the dynamical tides are important in evolved stars, and therefore both need to be taken into account when studying the tidal dissipation in evolved stars and the evolution of planetary or/and stellar companions orbiting them.

Key words. Planet-star interactions - Planetary systems - Binaries: close - Stars: evolution - Methods: numerical

1. Introduction

As more and more planets are being observed, they are also found around evolved stars. These planets are found in a wide range of orbital periods, ranging from a few days to a few years (e.g. Sato et al. 2008; Nowak et al. 2013; Döllinger & Hartmann 2021; Saunders et al. 2022; Lee et al. 2023; Pereira et al. 2024), or even a planet that is situated so close to its host star that it should have been swallowed by the star in earlier stages of its evolution (Hon et al. 2023). Not only planets around evolved stars have gotten more recent attention, also stellar companions have increasing importance. For instance, for Asymptotic Giant Branch (AGB) stars or planetary nebula, the presence of a binary companion is important in shaping the outflows of these stars (García-Segura et al. 2016; Decin et al. 2020). Binary stars have also been observed around post-AGB stars, where the orbital properties of these binaries show significant eccentricity, which is not predicted by current binary evolution models (Van Winckel 2003; Oomen et al. 2018). For these systems it is important to understand tidal effects during the late stages of stellar evolution, as tides play a significant role in the evolution of the orbital architecture of the system, as well as the rotational evo-

lution of the objects in the system (e.g. Ogilvie 2014; Bolmont & Mathis 2016; Mathis 2018; Ahuir et al. 2021b).

Tidal dissipation is a complex process characterized by two components: the equilibrium and dynamical tides. The former arises from the hydrostatic displacement induced by the ellipsoidal deformation triggered by a companion. The energy associated with the equilibrium tide is dissipated through turbulent friction in convective layers, leading to the transfer of angular momentum between the stellar spin and its orbital motion (Zahn 1966, 1989; Zahn & Bouchet 1989; Remus et al. 2012; Ogilvie 2013; Barker 2020). This well-established mechanism has been studied in various contexts, including investigations of observed Red Giant Branch (RGB) binaries (Verbunt & Phinney 1995; Beck et al. 2018, 2022, 2023), as well as theoretically for AGB binaries (Mustill & Villaver 2012; Madappatt et al. 2016; García-Segura et al. 2016), although these studies for AGB binaries use parameterised equations using fixed input parameters rather than ab-initio dissipation calculations. The dynamical tide involves tidal dissipation due to the excitation of stellar oscillations by the tidal potential. In the stellar convective zone, these waves are excited in the form of inertial waves that are restored by the Coriolis force (e.g. Wu 2005a,b; Ogilvie & Lin 2004, 2007), or in the

form of internal gravity waves (IGW) restored by the buoyancy in the radiative zone (e.g. [Zahn 1975](#); [Goldreich & Nicholson 1989](#); [Terquem et al. 1998](#); [Goodman & Dickson 1998](#); [Barker & Ogilvie 2010](#); [Ahuir et al. 2021a](#)). This dynamical tide dissipation varies over several orders of magnitude depending on the structure and the rotation of stars all along their evolution ([Mathis 2015](#); [Gallet et al. 2017](#); [Bolmont et al. 2017](#); [Barker 2020](#); [Ahuir et al. 2021a](#)). While tidal effects have been studied extensively in the pre-main-sequence (PMS) and main-sequence (MS), these dependence's have yet to be systematically evaluated along the evolved phases, despite its already identified crucial role for subgiants ([Weinberg et al. 2017](#); [Beck et al. 2018](#)) and RGB stars ([Ahuir et al. 2021a](#)). Therefore our focus in this investigation is on computing the tidal dissipation strengths in stars throughout their entire lifetime, with a particular emphasis on the evolved phases.

In this study, we bridge this gap by conducting a comprehensive investigation into the equilibrium and dynamical tide dissipation during the late stages of evolution. Utilising established theoretical frameworks and a grid of stellar evolution models with initial masses between 1 and $4 M_{\odot}$ to study of a range of stellar evolutionary effects such as the convective/radiative structure during the MS and presence of the helium flash. We aim to quantify and compare the dissipation strengths of the equilibrium and dynamical tides, providing a complete understanding of their contributions to the overall dissipation of tidal energy along the star's lifetime.

In Sect. 2, we provide an overview of the type of waves that can be excited in stars by tides, as well as an overview of the theoretical frameworks used to model the dissipation of the equilibrium and dynamical tides. In Sect. 3, we describe the stellar evolution models used in this study and their physical ingredients. In Sect. 4, we investigate both the dissipation of the equilibrium and dynamical tides along the evolution of stars as well as their relative strength. Finally, in Sect. 5 we provide the conclusions of this study.

2. Tidal dissipation modelling

In this section, we provide an overview of the theoretical frameworks used to compute the equilibrium and dynamical tides and their dissipation.

2.1. General framework

Considering two bodies, for instance a star and a planet, or two stars, where only the deformation of one object is considered, the gravitational potential of the secondary object can be expressed as a multipole expansion in spherical harmonics in the reference frame attached to the primary. The tidal potential is then given by the difference between the gravitational potential induced by the secondary object at each point of the extended primary body and its value at its center of mass and the first-order term ensuring the Keplerian motion. The tidal potential can be expressed as given in [Ogilvie \(2014\)](#):

$$\Psi(r, \theta, \varphi, t) = \text{Re} \left\{ \sum_{l=2}^{\infty} \sum_{m=0}^l \sum_{n=-\infty}^{\infty} \frac{GM_2}{a} A_{l,m,n}(e, i) \left(\frac{r}{a}\right)^l \times Y_l^m(\theta, \varphi) e^{-in\Omega_o t} \right\}, \quad (1)$$

where M_2 is the mass of the companion object (in g), a is the semi-major axis of the orbit (in cm), e is the eccentricity of the

orbit, i is the inclination of the orbit, r, θ, φ are spherical coordinates centred at the origin of the reference frame attached to the primary center of mass, Y_l^m are the spherical harmonics, $\Omega_o = \sqrt{G(M_1 + M_2)/a^3}$ is the orbital frequency (in rad/s), and $A_{l,m,n}$ are the tidal coefficients (see table 1 in [Ogilvie 2014](#)). In this study we focus on a coplanar circular orbit. In this case only the $l = m = n = 2$ terms are non-zero in the quadrupolar approximation ($l > 2$ is neglected; we refer the reader to [Mathis & Le Poncin-Lafitte 2009](#) for the conditions ruling this approximation), and the tidal potential can be expressed as:

$$\Psi = \text{Re} \left\{ \frac{GM_2}{a} \sqrt{\frac{6\pi}{5}} \left(\frac{r}{a}\right)^2 Y_2^2(\theta, \varphi) e^{-in\Omega_o t} \right\} \equiv \varphi_T(r) \text{Re} \left\{ Y_2^2(\theta, \varphi) e^{-in\Omega_o t} \right\}. \quad (2)$$

Since $Y_l^m \propto e^{im\varphi}$, the tidal potential has as complex argument $m\varphi - n\Omega_o t$. This means that the tidal potential rotates with a frequency $\omega_t = n\Omega_o - m\Omega_s$, where ω_t is the tidal frequency and Ω_s is the spin frequency of the star (in rad/s), which is assumed to be uniform here. This tidal frequency will be the characteristic frequency of the tidal waves excited in the star.

Tidal dissipation can be expressed through multiple formalisms, using for instance the tidal quality factor Q ([Kaula 1962](#)), the modified tidal quality factor Q' ([Ogilvie & Lin 2007](#)) or the Love number k_l^m ([Love 1911](#)). The tidal quality factor is defined as the ratio between the energy stored in the tidal bulge and the energy dissipated per orbit. The Love number is the ratio between the perturbation of the primary's gravitational potential induced by the presence of the companion and the tidal potential, evaluated at the stellar surface. The tidal quality factor and the Love number are related by

$$Q_l^m(\omega_t)^{-1} = \text{sgn}(\omega_t) \text{Im} [k_l^m(\omega_t)] / |k_l^m(\omega_t)| \quad (3)$$

and the modified tidal quality factor is related to the tidal quality factor and the Love number by

$$\frac{3}{2Q_l^m(\omega_t)} = \frac{k_l^m}{Q_l^m}. \quad (4)$$

Higher values of the imaginary part of the Love number indicate stronger tidal dissipation, while lower values of the tidal quality factor indicate stronger dissipation.

2.2. Tidal wave excitation

In order to understand the tidal dissipation in the primary star, it is important to understand what types of waves can be excited in the star, and more importantly what types of waves can be excited by the tidal potential. The tidal potential is a periodic potential, and therefore it can only excite waves with a frequency equal to the tidal frequency ω_t , the frequency at which the tidal potential rotates. If it is possible to excite waves at these frequencies, the excitation of these waves will drive the dynamical tide and the related dissipation and angular momentum exchanges. In this section the different types of waves that can be excited by tides in a primary evolved low or intermediate-mass evolved star are discussed, assuming a companion on a circular orbit at a distance of 1 AU.

2.2.1. Inertial waves

Inertial waves are waves that have the Coriolis force as a restoring force. These waves can only be excited in rotating stars

for sufficiently low frequencies in the regime $\omega \in [-2\Omega_s, 2\Omega_s]$ (Rieutord 2015). For tides to excite inertial waves this criterion holds if $\Omega_o < 2\Omega_s$. This means that for sufficiently slowly rotating stars, the tidal potential cannot excite inertial waves.

Stars with a convective envelope during the Main Sequence (MS) phase are spun down because of the magnetic braking by their pressure-driven winds (e.g. Skumanich 1972; Kawaler 1988). Therefore, if there is no sufficiently massive companion to spin up the star, the tidal potential cannot excite inertial waves during their subsequent evolution since inertial waves become less important already when progressing along the main-sequence (Mathis 2015; Gallet et al. 2017). Stars without a convective envelope during the MS don't experience this spin down, and are expected to still have significant rotation rates during their subsequent evolution. However, observations of these stars reveal low rotation rates during the RGB, the cause of which thought to be stronger rotational damping than predicted by models, or differential rotation within the star (Ceillier et al. 2017). Rotation during the AGB phase has been investigated theoretically but includes only the equilibrium tide. Rotation rates found in these studies predict sufficient spin up (but still low rotation rates) so that inertial waves can be excited for stellar mass companions (García-Segura et al. 2016; Madappatt et al. 2016), but not in the case of a Jupiter mass or lower-mass planetary companions (Madappatt et al. 2016).

Depending on the internal structure of the star, different types of inertial waves can be excited. When the star is fully convective, global normal modes can be excited (Wu 2005a,b), while stars with a radiative interior can excite wave attractors due to the reflection of the waves at the boundaries (at the so-called critical latitude) of the radiative zone (Ogilvie 2013). The strength of the dissipation of these waves depends on the Ekman number $E_k = \nu_t/(2\Omega_s R_\star^2)$, with ν_t the turbulent viscosity (in cm^2/s) and R_\star the radius of the primary star (in cm). For low Ekman numbers, the dissipation of these waves is strong, while for high Ekman numbers, the resonant dissipation of these waves is suppressed (Ogilvie & Lin 2004; Auclair Desrotour et al. 2015). For evolved stars, the Ekman number is typically on the order of 10^{-1} when calculated in our evolutionary models described in Sect. 3, assuming a turbulent viscosity as defined in Eq. (12) and a rotational period of 57 yr (Vlemmings et al. 2018). This is sufficiently high to suppress the resonant dissipation of these waves, and therefore the dissipation of these waves is not considered in this study.

2.2.2. Pressure waves

Pressure waves (p-waves) are waves that have pressure as their restoring force. These waves can be excited at frequencies higher than the Lamb-frequency $S_l = \frac{l(l+1)c_s^2}{r^2}$ (in Hz), with c_s being the local sound speed (Aerts et al. 2010, in cm/s). The Lamb-frequency variation for $l = 2$ as a function of radius is shown in Fig. 1 for a star with initial mass of $1 M_\odot$ during the RGB phase. Here the tidal frequency is also shown for a planet on a circular orbit at a distance of 1 AU. As can be seen, the tidal frequency is always lower than the Lamb-frequency ($\omega_t < S_l$), and therefore no pressure waves can be excited by the tidal potential. This conclusion holds for all stars within our considered mass range, and therefore the dissipation of pressure waves is not considered in this study.

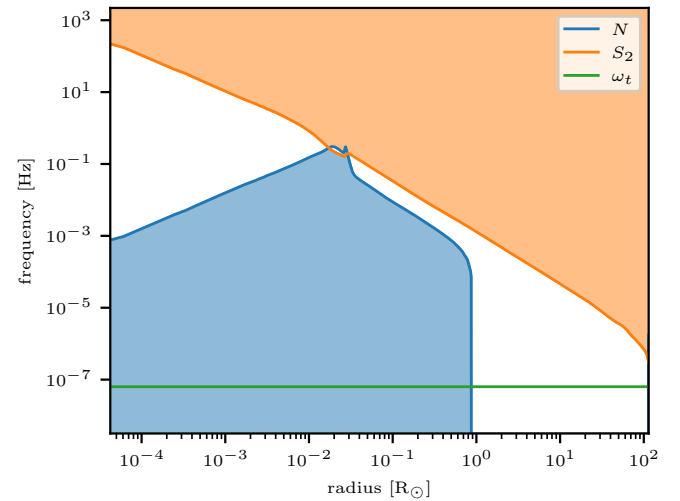


Fig. 1. The Brunt-Väisälä (N , in blue), Lamb (for $l = 2$; S_2 in orange) and tidal (ω_t in green) frequencies for a planetary companion orbiting an RGB star with $M_{\text{ZAMS}} = 1 M_\odot$ at a distance of 1 AU. The coloured regions indicate the regions where the different types of waves can be excited (see text for details).

2.2.3. Gravity waves

Gravity waves (g-waves) are waves that have buoyancy as their restoring force. These waves can be excited at frequencies lower than the Brunt-Väisälä frequency N (in Hz; Aerts et al. 2010):

$$N^2 = g_0 \left(\frac{\partial_r p_0}{\Gamma_1 p_0} - \frac{\partial_r \rho_0}{\rho_0} \right), \quad (5)$$

where g_0 , p_0 and ρ_0 are the unperturbed gravitational acceleration (in cm/s^2), pressure (in g/cm^2), and density (in g/cm^3) respectively. $\Gamma_1 = (\partial \ln p_0 / \partial \ln \rho_0)_S$ is the first adiabatic exponent, where S is the macroscopic entropy. This Brunt-Väisälä frequency is shown as a function of radius in Fig. 1 for a star with initial mass of $1 M_\odot$ during the AGB phase. Here the tidal frequency is also shown for a planet on a circular orbit at a distance of 1 AU. As can be seen, the tidal frequency is much lower than the maximal Brunt-Väisälä frequency ($\omega_t \ll N_{\text{max}}$), and therefore gravity waves in the form of internal gravity waves (IGW) can be excited by the tidal potential, and need to be taken into account when computing the dynamical tide and its dissipation.

Depending on the efficiency of the radiative damping, the waves are either damped before they can be reflected at the boundaries of the radiative zone, or they are reflected at the boundaries and travel back and forth through the radiative zone. The former type of waves are called progressive gravity waves, while in the latter case, the reflecting interaction of the waves create standing gravity modes. The two cases are separated by the critical frequency ν_c , which is the frequency at which the radiative damping is strong enough to damp the waves with a factor e before they can be reflected at the boundaries of the radiative zone. The critical frequency (in Hz) can be expressed as (Alvan et al. 2015):

$$\nu_c = [l(l+1)]^{\frac{3}{8}} \left(\left(\int_{r_{\text{in}}}^{r_{\text{out}}} K_T \frac{N^3}{r^3} dr \right)^{\frac{1}{4}} \right), \quad (6)$$

where K_T is the thermal diffusivity (in cm^2/s , calculated following Viallet et al. 2015). Frequencies lower than the critical fre-

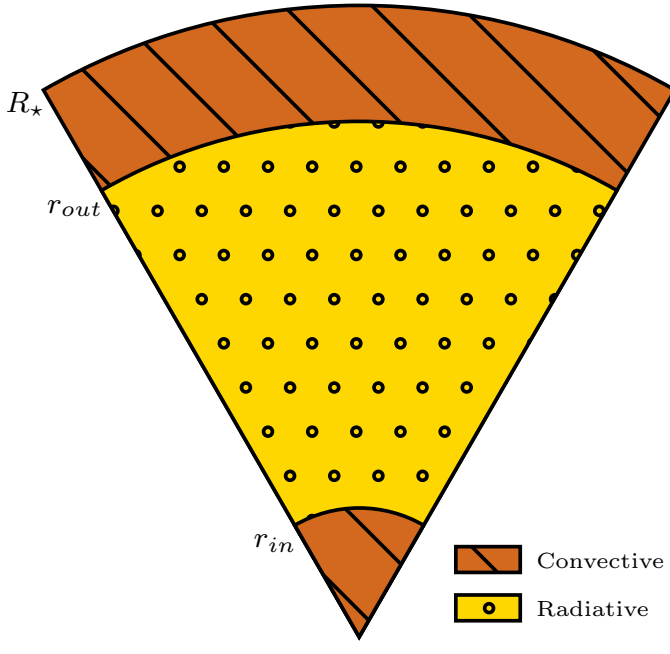


Fig. 2. Schematic representation of the radiative and convective shells in the case of the three-layer structure used in this study. Radii not up to scale for a real stellar structure (See Kippenhahn diagrams e.g. Fig. 5).

quency are progressive gravity waves, while frequencies higher than the critical frequency are gravity modes.

Here r_{in} and r_{out} are the inner and outer boundaries of the radiative zone assuming a three-layer structure (see Fig. 2). In the case there is only a radiative core and a convective envelope, $r_{\text{in}} = 0$ and $r_{\text{out}} = r_c$. In the case there is a convective core and a radiative envelope, $r_{\text{in}} = r_c$ and $r_{\text{out}} = R_\star$. In the case of a true three-layer structure (such as in MS F-type stars, or horizontal branch stars), one needs to be careful with this definition as waves starting at the inner boundary may interact with waves starting at the outer boundary, and still create g-modes while being in the progressive wave regime.

The critical frequency in evolved stars is lower than the tidal frequency (see Sect. 4.1), and therefore the tidal potential will mostly excite progressive gravity waves in evolved stars.

2.3. Tidal dissipation

2.3.1. Equilibrium tide

The equilibrium tide is the tidal dissipation originating from the hydrostatic deformation of an object due to the gravitational potential of a companion (Zahn 1966, 1989). The equilibrium tide is dissipated through turbulent friction in convective layers, leading to the transfer of angular momentum between the stellar spin and its orbital motion. In order to calculate the dissipation of the equilibrium tide, the tidal displacement of the star needs to be calculated. This displacement can be calculated by first computing the non-wavelike component of the gravitational potential Φ_l^{nw} which is obtained by solving the differential equation (e.g. Zahn 1966; Dhouib et al. 2023):

$$\frac{1}{r^2} \frac{d}{dr} \left(r^2 \frac{d\Phi_l^{\text{nw}}}{dr} \right) - \frac{l(l+1)}{r^2} \Phi_l^{\text{nw}} - 4\pi G \frac{d\rho_0}{dr} g_0 (\Phi_l^{\text{nw}} + \Psi_l) = 0 \quad (7)$$

for $l = 2$, where Ψ_l the tidal potential (in erg). Boundary conditions are chosen to ensure regularity at the center, and continuity

at the surface (Dhouib et al. 2023):

$$\begin{cases} \frac{d \ln \Phi_l^{\text{nw}}}{d \ln r} = l & \text{at } r = \eta R_\star \text{ for } \eta \rightarrow 0 \\ \frac{d \ln \Phi_l^{\text{nw}}}{d \ln r} = -(l+1) & \text{at } r = R_\star \end{cases} \quad . \quad (8)$$

When the non-wavelike component of the gravitational potential is known, the tidal displacement (in cm, radial r and horizontal h components) can be calculated following (Zahn 1966; Remus et al. 2012; Dhouib et al. 2023) to ensure the equilibrium tide continuity at each radiative/convective boundary:

$$\xi_{r,l}^{\text{nw}} = -\frac{\Phi_l^{\text{nw}} + \Psi_l}{g_0}, \quad \xi_{h,l} = \frac{1}{l(l+1)} \left(2\xi_{r,l}^{\text{nw}} + r \frac{d\xi_{r,l}^{\text{nw}}}{dr} \right). \quad (9)$$

Then using these expressions we compute the dissipation of the equilibrium tide following Barker (2020):

$$[\text{Im } k_2^2]_{\text{eq}} = \frac{16\pi G \omega_t}{4(2l+1)R_\star^{2l+1} |\varphi_T(R_\star)|^2} \int_0^{R_\star} r^2 \nu_t D_l(r) dr, \quad (10)$$

with

$$D_l(r) = \left(3 \frac{d\xi_{r,l}^{\text{nw}}}{dr} - \frac{1}{r^2} \frac{d(r^2 \xi_{r,l}^{\text{nw}})}{dr} + l(l+1) \frac{\xi_{h,l}^{\text{nw}}}{r} \right)^2 + l(l+1) \left(\frac{\xi_{r,l}^{\text{nw}}}{r} + r \frac{d(\xi_{h,l}^{\text{nw}}/r)}{dr} \right)^2 + (l-1)l(l+1)(l+2) \left(\frac{\xi_{h,l}^{\text{nw}}}{r} \right)^2, \quad (11)$$

where $l = 2$ and $\nu_t(x)$ the turbulent viscosity (in cm^2/s) given by Duguid et al. (2020):

$$\nu_t = V_c l_c F(\omega_t), \quad F(\omega_t) = \begin{cases} 5 & |\omega_t| t_c < 10^{-2} \\ \frac{1}{2} (|\omega_t| t_c)^{-\frac{1}{2}} & |\omega_t| t_c \in [10^{-2}, 5] \\ \frac{25}{\sqrt{20}} (|\omega_t| t_c)^{-2} & |\omega_t| t_c > 5 \end{cases} \quad (12)$$

with V_c the convective velocity (in cm/s), l_c the mixing length (in cm), and t_c the convective turnover time (in s).

2.3.2. Dynamical tide for progressive IGW

Additionally to the equilibrium tide is the dynamical tide, constituted here by progressive internal gravity waves. These waves are excited with the frequency being the tidal frequency ω_t . These IGW are dissipated through radiative damping, leading to the transfer of angular momentum between the stellar spin and its orbital motion (e.g. Zahn 1975; Goldreich & Nicholson 1989).

Assuming the three-layer structure (see Fig. 2), the tidal dissipation can be calculated for waves emerging from the convective core and the convective envelope, as formulated by Ahuir et al. (2021a) (we refer the reader to this article for the details of the theoretical calculations leading to this expression):

$$[\text{Im } k_2^2]_{\text{IGW}} = \frac{3^{-\frac{1}{3}} \Gamma^2 \left(\frac{1}{3} \right)}{4\pi} m [l(l+1)]^{-\frac{4}{3}} \frac{\omega_t^{\frac{8}{3}}}{\Omega_o^4} \frac{GM_1^2}{M_2^2 R_\star^5} \times \left(\rho_0(r_{\text{in}}) r_{\text{in}} \left| \frac{dN^2}{d \ln r} \right|_{r_{\text{in}}}^{-\frac{1}{3}} \mathcal{F}_{\text{in}}^2 + \rho_0(r_{\text{out}}) r_{\text{out}} \left| \frac{dN^2}{d \ln r} \right|_{r_{\text{out}}}^{-\frac{1}{3}} \mathcal{F}_{\text{out}}^2 \right) \quad (13)$$

with \mathcal{F}_{out} and \mathcal{F}_{in} being the tidal forcing (in cm^2) at the inner and outer boundary of the radiative zone, and Γ the gamma function (Abramowitz & Stegun 1972). The tidal forcing term at the inner and outer boundary of the radiative zone can be expressed as (Ahuir et al. 2021a):

$$\begin{aligned}\mathcal{F}_{\text{in}} &= \int_0^{r_{\text{in}}} \left[\left(\frac{r^2 \varphi_T}{g_0} \right)'' - \frac{l(l+1)}{r^2} \left(\frac{r^2 \varphi_T}{g_0} \right) \right] \frac{X_{1,\text{in}}}{X_{1,\text{in}}(r_{\text{in}})} dr \\ \mathcal{F}_{\text{out}} &= \int_{r_{\text{out}}}^{R_*} \left[\left(\frac{r^2 \varphi_T}{g_0} \right)'' - \frac{l(l+1)}{r^2} \left(\frac{r^2 \varphi_T}{g_0} \right) \right] \frac{X_{1,\text{out}}}{X_{1,\text{out}}(r_{\text{out}})} dr,\end{aligned}\quad (14)$$

where $X_{1,\text{out}}$ and $X_{1,\text{in}}$ are representations for the radial displacement originating from the inner and outer boundary of the radiative zone, and φ_T is defined in Eq. (2). The radial displacement can be calculated using the following differential equations and boundary conditions (Ahuir et al. 2021a):

$$\begin{cases} X_{1,\text{out}}'' - \frac{\partial_r \rho_0}{\rho_0} X_{1,\text{out}}' - \frac{l(l+1)}{r^2} X_{1,\text{out}} = 0 \\ X_{1,\text{out}}(r)_{r \rightarrow 0} \propto r^{1/2 + \sqrt{1/4 + l(l+1)}} \\ X_{1,\text{out}}'(r)_{r \rightarrow 0} \propto (1/2 + \sqrt{1/4 + l(l+1)}) r^{-1/2 + \sqrt{1/4 + l(l+1)}} \\ X_{1,\text{in}}'' - \frac{\partial_r \rho_0}{\rho_0} X_{1,\text{in}}' - \frac{l(l+1)}{r^2} X_{1,\text{in}} = 0 \\ X_{1,\text{in}}(r)_{r \rightarrow R_*} \propto \rho_0 \left(r - R_* - \frac{\varphi_T(R_*)}{g_0(R_*)} \right) \\ X_{1,\text{in}}'(r)_{r \rightarrow R_*} \propto \rho_0(R_*) \end{cases}\quad (15)$$

where the proportionality factor in the boundary conditions is cancelled out as X is always rescaled to the interaction region $X/X(r_{\text{int}})$ in Eq. (14). The boundary conditions are calculated by assuming that $\frac{\partial_r \rho_0}{\rho_0}$ is small close to the center of the star, and that $\frac{l(l+1)}{r^2}$ is small close to the surface of the star in the case of the studied coplanar circular orbit of the companion for which $l = m = 2$.

3. Stellar evolution models

To study the different tidal dissipation mechanisms throughout a star's lifetime, stellar evolutionary models are necessary. In this study we use the Modules for Experiments in Stellar Astrophysics (MESA) code (Paxton et al. 2011, 2013, 2015, 2018, 2019; Jermyn et al. 2023) to calculate these stellar evolutionary models. Models are computed for Zero Age Main Sequence (ZAMS) masses between 1 and $4 M_\odot$ at solar metallicity ($Z = 0.0134$; Asplund et al. 2009) for which the Hertzsprung-Russell (HR) diagram is shown in Fig. 3¹. These masses are chosen to allow the study of a range of stellar evolutionary effects such as the difference between a convective or radiative envelope during the MS and the difference between a helium flash or gradual helium burning. The models are computed from the pre-main-sequence (PMS) up to the white dwarf (WD) stage. The models are terminated when the WD is cooled down sufficiently to have a luminosity of $L = 10^{-1} L_\odot$.

To simulate convection, the Mixing Length Theory (MLT) is used following the prescription of Henyey et al. (1965). In this prescription α_{MLT} is the mixing length parameter, which is calibrated by Cinquegrana & Joyce (2022) to reproduce the solar radius and luminosity at the solar age, resulting in $\alpha_{\text{MLT}} = 1.931$.

¹ The inlist used to compute the stellar evolutionary models can be found both in App. C and zenodo: url (to be done)

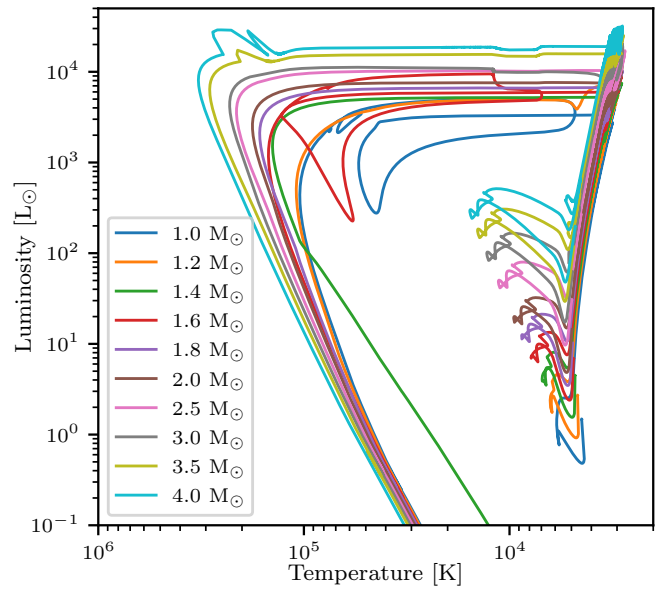


Fig. 3. Hertzsprung-Russell diagram of the stellar evolutionary models studied here. The models start in the pre-main-sequence and are evolved up to the white dwarf phase. Different colors indicate a different ZAMS mass, as indicated in the box in the left-bottom corner of the figure.

As evolved stars have relative low temperatures, a dedicated low-temperature molecular opacity table (ÆSOPUS, Marigo & Aringer 2009) is used. For the atmosphere, a grey temperature-opacity ($T - \tau$, where τ is the optical depth) relation is assumed, based on the Eddington relation (Paxton et al. 2011).

The mass-loss rate is calculated using the Reimers prescription (Reimers 1975) during the RGB phase, with a scaling factor of $\eta_{\text{Reimers}} = 0.477$ (McDonald & Zijlstra 2015). Later on, during the AGB phase, the Blöcker prescription (Blöcker 1995) is used, with a scaling factor of $\eta_{\text{Blöcker}} = 0.05$ for masses below $2 M_\odot$ and $\eta_{\text{Blöcker}} = 0.1$ for masses above $2 M_\odot$ (Madappatt et al. 2016).

Stars undergo internal mixing, which is described by convective mixing in the convective zone. Radiative layers are also the seat of mild mixing and transport mechanisms (see e.g. Zahn 1992; Mathis 2013; Aerts et al. 2019). To have a simple description of the mixing in the radiative zone, we assume a constant uniform mixing coefficient $D_{\text{min}} = 10 \text{ cm}^2 \text{ s}^{-1}$ throughout the radiative layers. Multiple values were tested for D_{min} , and the resulting tidal dissipation was found to be insensitive to the exact value of D_{min} . This value was chosen to help numerical stability within the MESA simulations.

4. Tidal dissipation along stellar evolution

During the evolution of the star, the strength of tidal dissipation varies due to the changes in internal structure and rotation (e.g. Mathis 2015; Gallet et al. 2017; Bolmont et al. 2017; Barker 2020; Ahuir et al. 2021a). In this section, we investigate the tidal dissipation along the stellar evolution, focusing specifically on advanced stages from the RGB to the WD stages. To verify our results, we benchmark them with the values of the dissipation of the equilibrium and dynamical tides found in Ahuir et al. (2021a) who computed the equilibrium and dynamical tide dissipation up to the RGB phase. The comparison was done for the 1, 1.2 and $1.4 M_\odot$ stars in App. A. We find good agreement between

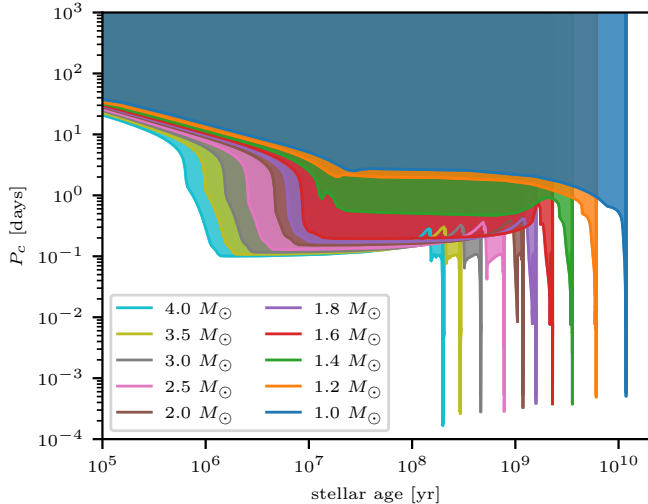


Fig. 4. The critical period $P_c = 1/\nu_c$ for different stellar masses. The color represents the same model as in Fig. 3. The coloured regions indicate the regions where the gravity waves are excited as progressive internal gravity waves.

our results and the results of Ahuir et al. (2021a). Before going into detail on the tidal dissipation, the validity of our formalism is checked, by investigating the critical period as a function of stellar mass.

4.1. Critical period

The critical period ($P_c = 1/\nu_c$; Eq. 6) as a function of stellar age is shown in Fig. 4 for all stellar evolutionary models used in this study. During the PMS, the critical period is high (higher than a few days), and decreases when the MS starts. During the MS, the critical period remains approximately constant, and decreases when the RGB phase starts. Afterwards the critical period remains low (lower than 0.1 day). This means that our formalism is valid for stars along the evolved phases.

The critical period also depends on the initial mass of the star. For lower mass stars (e.g. the $1 M_\odot$ model), the critical period is approximately 3 days during the MS, while for higher mass stars (e.g. the $4 M_\odot$ model), the critical period is approximately 0.1 days during the MS. Therefore it is possible for short period companions around the lower mass stars (below $1.4 M_\odot$) in the MS to excite g-modes in the radiative layer instead of progressive internal gravity waves. The tidal dissipation of these g-modes is likely to be more effective than the tidal dissipation estimated in this study, since standing modes might experience enhanced dissipation efficiency, potentially amplified through resonance locking (e.g. Witte & Savonije 2002; Fuller 2017).

4.2. Earth around the Sun

4.2.1. Internal structure of a $1 M_\odot$ star

Tidal dissipation depends strongly on the internal structure of the star. Fig. 5 shows the Kippenhahn of a $M_{\text{ZAMS}} = 1 M_\odot$ star. Here the stellar age is represented as time until the end of the simulation, hence the time until the WD is cooled down to produce a luminosity of $L = 10^{-1} L_\odot$. When plotting this time in logarithmic scale, the evolved phases can be shown in a single plot. The different evolutionary phases are indicated in Fig. 5.

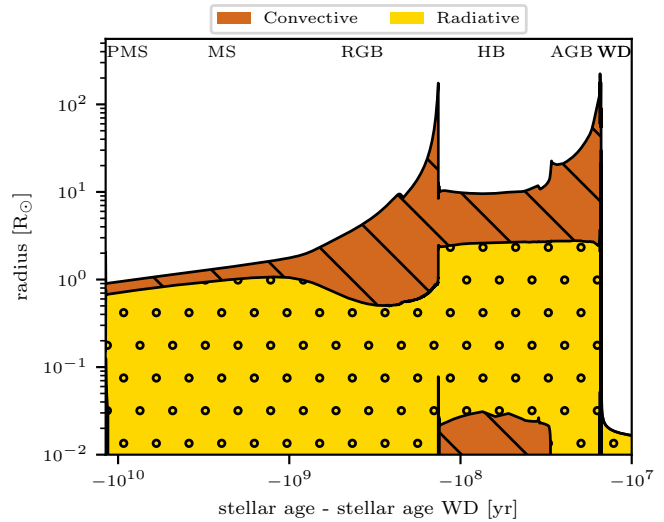


Fig. 5. Kippenhahn diagram for a $M_{\text{ZAMS}} = 1 M_\odot$ star. The brown hatched region represents convective layers and the yellow dotted region represents radiative layers. The upper layer represents the radius of the star. All stellar evolutionary phases (PMS to WD) are shown, and indicated in the figure.

During the MS, the radius increases gradually, where the star has a convective envelope and a radiative core. After the MS, the star starts to expand rapidly, and the convective envelope grows. During the RGB phase, the star has a convective envelope and a radiative interior. When the star reaches the tip of the RGB, the star contracts during the helium flash, where the radius of the star stays relatively constant during the horizontal branch (HB). During this phase, the star has a convective core, creating a three-layer structure. After the HB, the star expands again, and the star has a convective envelope and a radiative core in the AGB phase. When the star reaches the tip of the AGB, the star contracts again, and the star leaves the AGB track to cool down as a WD. During the WD phase, the star has a radiative interior.

4.2.2. Tidal dissipation

Considering a planet with an orbit of 1 yr and the mass of the Earth (e.g. the Earth), which is rotating around such a star with an initial mass of $1 M_\odot$ (e.g. the Sun). For simplicity the orbit is assumed to remain at a period of 1 yr. In Fig. 6, we compute the evolution of the imaginary part of the Love number both for the equilibrium and dynamical tides as a function of time. Looking at the equilibrium tide in the figure, the Love number follows the trend of the radius quite well. When the radius increases, the Love number increases, and vice versa. This is due to the fact that for stars with a larger radius, the local gravity is weaker, and therefore the star is more easily deformed by the tidal potential. This results in larger values of ξ_r and ξ_h , and a larger integral in Eq. (10). This is compensated by the direct dependence of $R^{-(2l+1)}$, but the dependence on ξ_r and ξ_h (which are dependant on R_\star^2 and appear squared in the equilibrium tide dissipation), and the integral (due to the r^2 in the equation this is dependant on R_\star^3) wins.

This is not the case for the dynamical tide. To explain the complex behaviour of its dissipation, the different components appearing in the dissipation of the dynamical tide (Eq. 13) are shown as a function of stellar age in Fig. 7. The change in radius

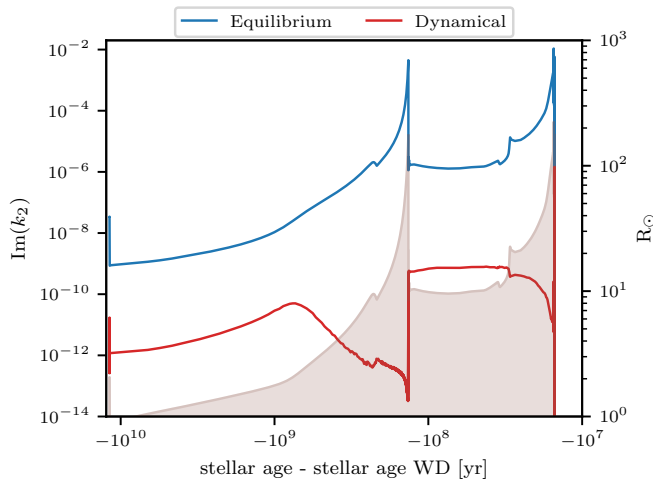


Fig. 6. On the left axis the complex part of the Love number ($\text{Im}(k_2)$) for both equilibrium (blue) and dynamical (red) tides is shown as function of stellar age for a $M_{\text{ZAMS}} = 1 M_{\odot}$ star with a $1 M_{\text{Earth}}$ companion at 1 AU. On the right axis the stellar radius is shown in light brown.

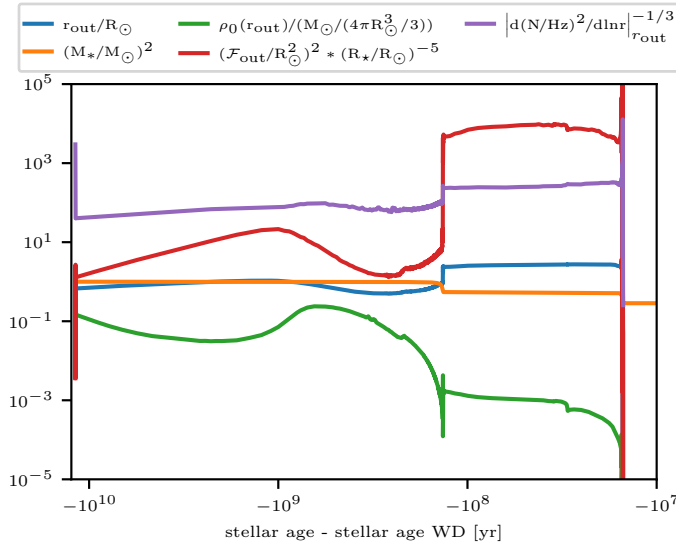


Fig. 7. Different components appearing in the dissipation of the dynamical tide (Eq. 13) as a function of stellar age. The change in radius of the radiative-convective boundary is represented in blue, the change in stellar mass in orange, the change in local density at the boundary in green, the change in tidal forcing compared to changes in stellar radius in red, and change in the derivative of the Brunt-Väisälä frequency in purple.

of the radiative-convective boundary is represented in blue, the change in stellar mass in orange, the change in local density at the radiative-convective boundary in green, the change in tidal forcing compared to changes in stellar radius in red, and change in the derivative of the Brunt-Väisälä frequency in purple. The change in radius of the radiative-convective boundary, change in stellar mass and change in the derivative of the Brunt-Väisälä frequency are small compared to the changes in the tidal forcing and local density at the boundary. This is due to the low power of the Brunt-Väisälä frequency and radius of the boundary and the small change in the stellar mass. The dissipation is proportional

to R_{\star}^{-5} , and thus the dynamical tide dissipation responds inversely to an increase in radius². This effect is compensated by the tidal forcing \mathcal{F} which depends on φ_T that scales as R_{\star}^2 . When multiplying their contributions, a complex pattern appears (as can be seen in red in Fig. 7). First this multiplied component increases, as the star increases while the size of the convective envelope remains approximately constant. When the convective envelope starts to becomes thicker at the start of the RGB, the tidal forcing grows slower than the stellar radius increases, as $X(r)/X_{\text{out}}$ decreases as X_{out} increases for larger sizes of the convective envelope, and therefore the multiplied component decreases. At the same time the local density at the boundary layer decreases as well, due to the large extend (and thus low density) of the envelope. This combination results in a dissipation of the dynamical tide that first increase during the subgiant phase and at the start of the RGB (in agreement with Ahuir et al. 2021a) and then decrease during the RGB (see Fig. 6). When the helium flash occurs and the star contracts, the extent of the radiative core increases again, and therefore the tidal forcing increases. For that reason, the dynamical tide dissipation increases during the HB. Additionally the star has a small convective core in this phase, and there is a contribution from the inner boundary of the radiative zone to the tidal dissipation, but this component is negligible compared to the contribution from the outer boundary. During the HB the internal structure remains approximately constant, and therefore the tidal dissipation remains approximately constant. When the star starts to expand during the AGB, the size of the radiative core remains approximately constant, and therefore the multiplied component remains approximately constant as well. However, as the stellar radius grows, and therefore the density at the boundary layer decreases, the dynamical tide dissipation decreases in strength. During the WD phase, the star is fully radiative, and therefore there is no convective region where the tidal forcing can grow. In this case our formalism does not apply, and the dynamical tide can excite standing gravity modes (Fuller & Lai 2011, 2012, 2013, 2014) for stellar companions or f-modes (Veras & Fuller 2019) for planetary companions. These dynamical tides are not calculated in this study.

Overall the tidal dissipation of the equilibrium tide is dominant compared to the dissipation of the dynamical tide at this orbital period. But as they have different dependencies this will change for different orbital periods and different primary and secondary masses, as will be shown in the next sections.

4.3. Dependence of tidal dissipation on orbital period

The strength of the equilibrium and dynamical tides are dependent on the orbital distance. For the equilibrium tide dissipation this is captured in the linear dependence on ω_t , but there is also a complex dependence of the turbulent viscosity on ω_t (see Eq. 12). For the dynamical tide dissipation there is a dependence in ω_t , n , the tidal forcing, and the boundary conditions of X . This results in a complex dependence on orbital period which is investigated for a $1 M_{\odot}$ star.

4.3.1. Equilibrium tide

The dissipation of the equilibrium tide as a function of stellar age and orbital period is shown in Fig. 8. When a companion is

² Note that although the Love number is dependent on R_{\star}^{-5} , when calculating the change of the semi-major axis of the orbit throughout time there is an additional factor of R_{\star}^5 cancelling out this direct dependence on stellar radius.

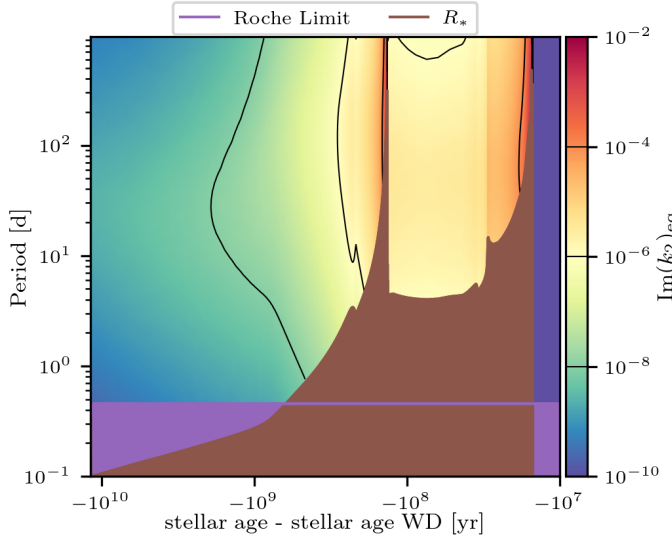


Fig. 8. Complex part of the Love number for the equilibrium tide ($\text{Im}(k_2)_{\text{eq}}$) as a function of the orbital period and stellar age, for a $M_{\text{ZAMS}} = 1 M_{\odot}$ star. R_{\star} (in brown) represents the orbital period for which a planet orbits at the surface the star, and the Roche limit is given in purple.

too close to the star, the companion will be destroyed by tidal forces. This is represented by the Roche limit, which is shown in Fig. 8 in purple (for the details of its calculation, we refer to Benbakoura et al. 2019). Here it can be seen that by increasing the orbital period, the equilibrium tide dissipation increases until a maximum is reached, after which the equilibrium tide dissipation becomes weaker again. The reason is that for low orbital periods, the tidal frequency is sufficiently high such that in the dominant region (the region where most of the dissipation occurs) the turbulent viscosity is proportional to the inverse square of the tidal frequency. Because there is an additional linear dependence of the tidal frequency on the Love number of the equilibrium tide, the dissipation of the equilibrium tide is proportional to the inverse of the tidal frequency, and hence will increase with increasing orbital period. However, when the orbital period is sufficiently high, the tidal frequency times the convective time t_c becomes sufficiently (see Eq. 12) such that the turbulent viscosity is proportional to the inverse square root of the tidal frequency, and thus the dissipation of the equilibrium tide is proportional to the square root of the tidal frequency. Therefore, by increasing the orbital period further, the equilibrium tide dissipation will decrease.

4.3.2. Dynamical tide

The dynamical tide dissipation as a function of stellar age and orbital period is shown in Fig. 9. Here it can be seen that by increasing the orbital period, the dynamical tide dissipation strictly decreases. Looking at Eq. (13), there is a dependence on ω_t , n , the tidal forcing, and the boundary conditions of X . The tidal forcing is proportional to the inverse of the square of the orbital period (as there is φ_T , which has a dependence of $a^3 \propto n^{-2}$). Hence, this cancels out the direct dependence on the orbital frequency in the equation. The dependence in the boundary condition of X on the orbital period (again due to φ_T) remains small, and only has a small effect at low orbital periods. The dependence on $\omega_t^{8/3}$ is the dominant factor, and thus the dynamical tide

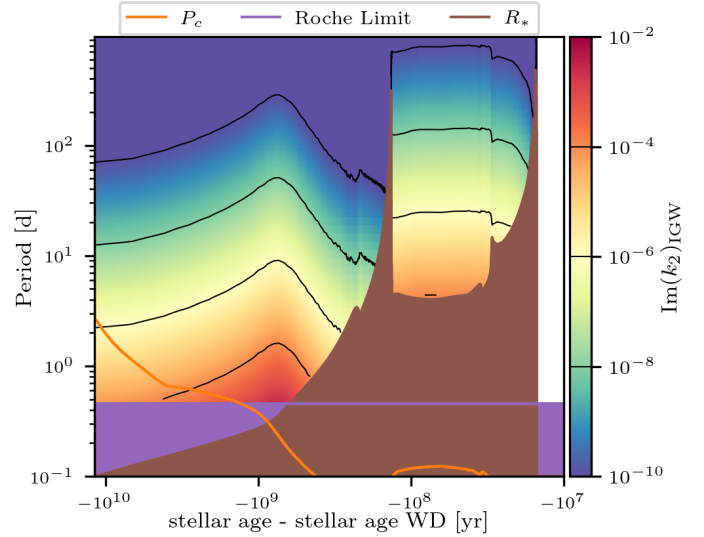


Fig. 9. Complex part of the Love number for the dynamical tide ($\text{Im}(k_2)_{\text{IGW}}$) as a function of orbital period and stellar age, for a $M_{\text{ZAMS}} = 1 M_{\odot}$ star. The critical period P_c is shown in orange, for which planets orbiting above this period excite progressive internal gravity waves. R_{\star} (in brown) represents the orbital period for which a planet orbits at the surface the star, and the Roche limit is given in purple.

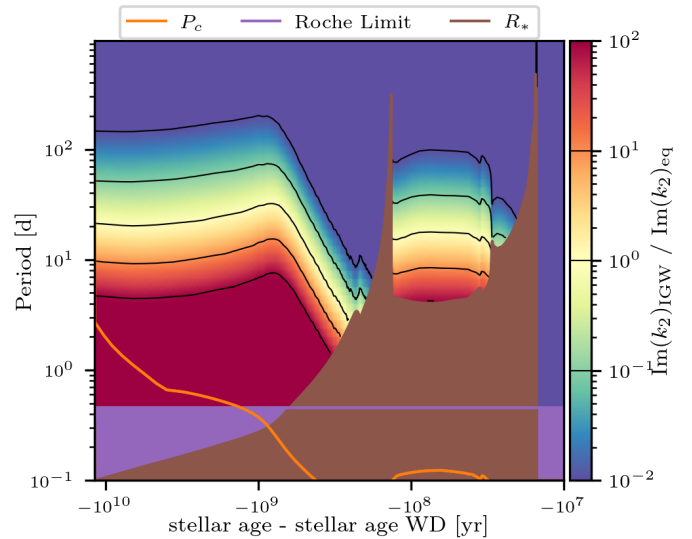


Fig. 10. Ratio of the complex parts of the Love number for the dynamical to equilibrium tide ($\text{Im}(k_2)_{\text{IGW}} / \text{Im}(k_2)_{\text{eq}}$) as a function of orbital period and stellar age, for a $M_{\text{ZAMS}} = 1 M_{\odot}$ star. The critical period P_c is shown in orange, for which planets orbiting above this period excite progressive internal gravity waves. R_{\star} (in brown) represents the orbital period for which a planet orbits at the surface the star, and the Roche limit is given in purple.

dissipation is proportional to $P_{\text{orb}}^{-8/3}$. At the end of the star's evolution, when the star is a WD and the star is fully radiative, the dynamical tide is not calculated as our formalism does not hold. Therefore this region is left blank in Fig. 9. In this region, the dynamical tide can excite standing g-modes and f-modes (Fuller & Lai 2011, 2012, 2013, 2014; Veras & Fuller 2019) and thus will have a different dependence on orbital period.

4.3.3. Relative strengths

Since the strengths of the equilibrium and dynamical tide dissipation have a different dependence on stellar age and orbital period, the dissipation of the equilibrium tide will be dominant in some regions of the parameter space, while in other regions, the dissipation of the dynamical tide will be more important. This can be seen in Fig. 10, where their ratio is shown. During the MS, the dynamical tide dissipation is dominant for orbits shorter than a few days in agreement with previous work (Ahuir et al. 2021a). There is a gradual change until orbital periods longer than 100 days where the equilibrium tide dissipation dominates. When the star enters the RGB, the equilibrium tide dissipation increases, while the dynamical tide dissipation decreases (see Sect. 4.2.2), resulting in the equilibrium tide dissipation becoming dominant for shorter orbital periods, and dominating completely when the star is sufficiently large. When the star contracts and becomes a HB star, the dynamical tide dissipation becomes stronger, remaining relevant again for orbits up to a 100 days. When the star enters the AGB, the equilibrium tide dissipation becomes dominant again, similar to the RGB phase. When the star contracts to become a WD, the star becomes fully radiative and our formalism cannot be applied anymore. Then, the dissipation of the equilibrium tide dominates. However, in such a configuration tidal g- and f- modes can be excited and their dissipation may dominate the one of the equilibrium tide.

4.4. Dependence of tidal dissipation on secondary mass

The dependence of the tidal dissipation on the secondary mass is complex, and is dependent on whether we assume the orbital period and orbital distance to vary as a function of this parameter or not. Let's first assume both the orbital period and distance to be constant, a good approximation when only varying companion mass, which is negligible compared to the mass of the primary star as in the case of the planet. Then, the relation between the semi-major axis and the orbital period has only a weak dependence on the secondary mass. In this situation, there is a dependence on the secondary mass via φ_T and D_l , with φ_T being proportional to M_2 and D_l being proportional to M_2^2 . Therefore, the equilibrium tide dissipation given in Eq. (10) is independent of the mass of the companion. For the dynamical tide dissipation (Eq. 13), there is direct dependence on the secondary mass, as well as in \mathcal{F} which contains φ_T . The direct dependence on the mass of the companion cancels out again. This is expected as the Love number is defined as the ratio between the perturbation of the primary's gravitational potential induced by the presence of the companion and the tidal potential, evaluated at the stellar surface, and the direct dependence of the secondary mass in both the numerator and denominator is the same, resulting in a constant Love number.

However when the companion becomes more massive, the relation between the orbital period and the orbital distance ($a^3/P^2 = G(M_1+M_2)/4\pi^2$) becomes dependent on the secondary mass, altering the Love number in a non-trivial way. Let's now consider the situation where the orbital period is fixed. Then, the semi-major axis changes proportional to $\sqrt[3]{M_1+M_2}$. Given the fact that the tidal forcing \mathcal{F} is inversely dependent on the semi-major axis cubed ($\mathcal{F} \propto a^{-3}$) as it depends on φ_T (see Eq. 2), the tidal forcing is weaker by a factor $(M_1+M_2)/M_1$ compared to a companion with a small (negligible) mass. This results in the dynamical tide dissipation being weaker with a factor $((M_1+M_2)/M_1)^2$ for higher mass companions for the same orbital period.

On the other hand when fixing the semi-major axis a , but allowing the orbital period to vary by changing the secondary mass, the orbital frequency and thus the tidal frequency will change, with the orbital period being proportional to $1/\sqrt{M_1+M_2}$. Since the semi-major axis remains constant in this situation, the tidal forcing remains constant as well. Therefore the dynamical tide dissipation will be proportional to $\omega_t^{8/3}/\Omega_0^4$ and thus proportional to $P^{4/3}$. For higher mass companions, the dynamical tide dissipation will become weaker with a factor $((M_1+M_2)/M_1)^{2/3}$. In this case the equilibrium tide dissipation will be affected as well as there is a linear dependence on the tidal frequency. For higher mass companions, the equilibrium tide dissipation will become stronger with a factor $\sqrt{(M_1+M_2)/M_1}$.

4.5. Dependence of tidal dissipation on primary mass

The strength of the dissipation of the equilibrium and dynamical tides are dependent on the mass of the primary star and the evolutionary stage. In this section we investigate the dependence of the tidal dissipation on the primary stellar mass and age using the grid of stellar models with initial masses between 1 and 4 M_\odot . The Kippenhahn diagram, together with the complex part of the Love number for both the equilibrium and dynamical tides as well as the ratio of their dissipation as a function of stellar age and orbital period, are shown in Figs. 11, 12 and 13, as well as in App. B.

4.5.1. Changes during the MS and RGB

When stars start their evolution with different initial masses, the internal structure on the MS changes. Lower mass stars have a convective envelope and a radiative interior (like the $1 M_\odot$ star). Higher mass stars have a convective core and a radiative envelope, like for instance a $2 M_\odot$ star (see Fig. 11). In our models the transition between these two structures happens at a mass of $1.4 M_\odot$ (see Fig. B.2). For higher mass stars with a radiative envelope (the star still has a tiny convective envelope at the surface of the star), the equilibrium tide dissipation is drastically reduced, as well as the dynamical tide dissipation arising from the tiny convective envelope. At this point, the dynamical tide arising from the convective core propagating in the radiative envelope becomes dominant for short orbital periods (in agreement with Zahn 1975, 1977; Goldreich & Nicholson 1989). This dominance over the equilibrium tide dissipation is less pronounced compared to the $1 M_\odot$ star. This dynamical tide arising from the convective core decreases during the MS, as the size of the convective core is reduced during this phase, while at the same time the radius increases. When these stars evolve into RGB stars, the convective envelope reappears, and the equilibrium tide dissipation from this region and the dynamical tide excited at the boundary between the radiative core and the convective envelope become dominant again. This results in a sudden increase in the ratio of the dissipation of the dynamical to equilibrium tide, where afterwards it decreases similar to the $1 M_\odot$ star.

4.6. Changes during the HB and AGB

When stars evolve from the RGB into the HB, they will go through a helium flash for low mass stars (up to $M_{\text{ZAMS}} = 2 M_\odot$), while for intermediate mass stars (above $2 M_\odot$) the burning of helium starts gradually. For low mass stars, this results in a sudden contraction of the star, and a sudden increase in the

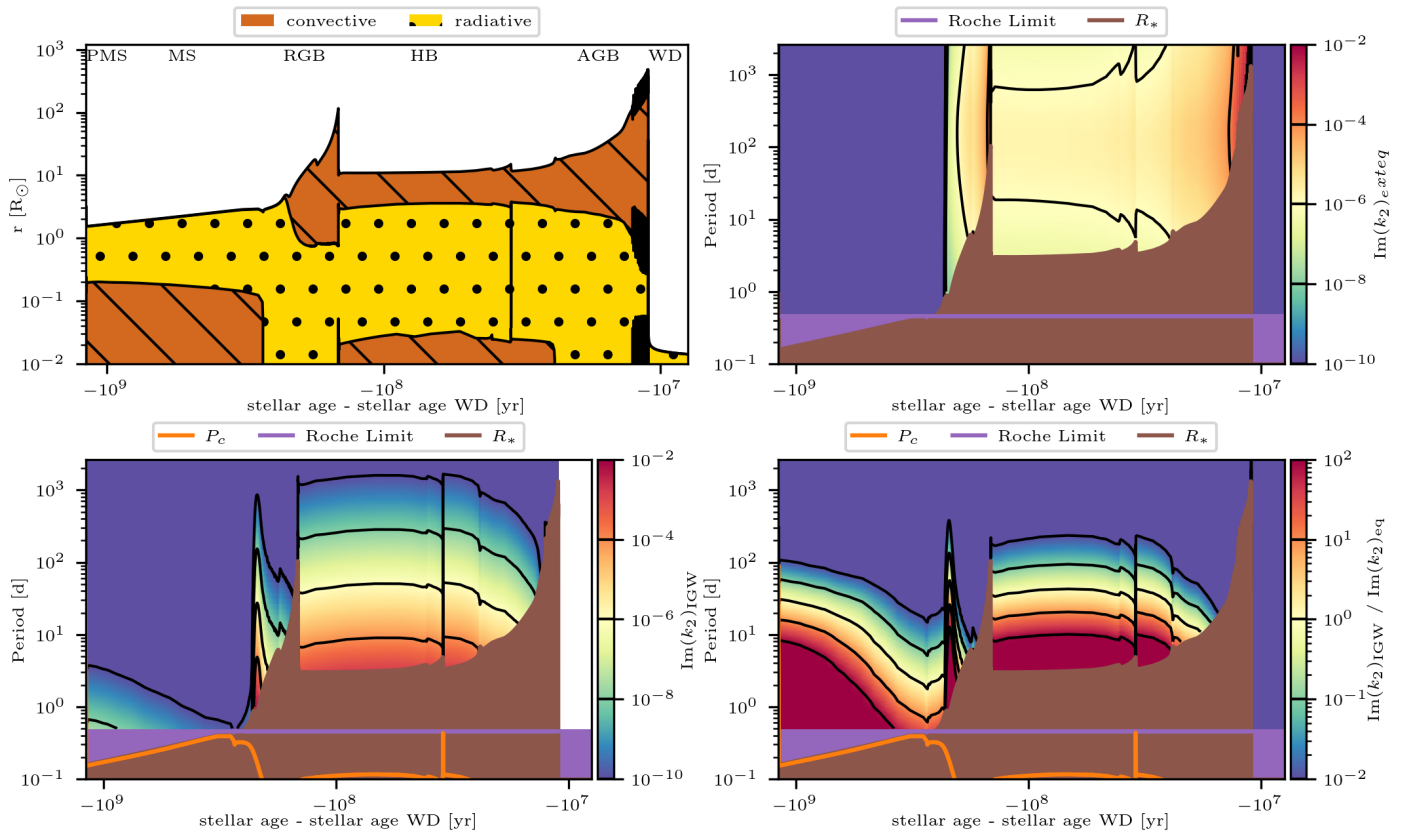


Fig. 11. Figures for a $M_{\text{ZAMS}} = 2 M_{\odot}$ star. On the top left a Kippenhahn diagram is shown, where the brown hatched regions represents convective layers and the yellow dotted region represents radiative layers. On the top right, bottom left and bottom right the complex part of the Love number for the equilibrium tide ($\text{Im}(k_2)_{\text{eq}}$), the dynamical tide ($\text{Im}(k_2)_{\text{IGW}}$) and the ratio of the dissipation's of the dynamical tide to the dissipation of the equilibrium tide ($\text{Im}(k_2)_{\text{IGW}} / \text{Im}(k_2)_{\text{eq}}$) are shown, respectively, as a function of stellar age and orbital period. Here the Roche limit is shown in purple, the critical period ($1/v_c$, see Eq. 6) in orange, and the period at which a planet orbits at the stellar radius in brown.

ratio of the dissipation of the dynamical to equilibrium tide (see Sect. 4.2.2). For intermediate mass stars, the star will slowly contract, resulting in a slow increase of this ratio.

The length of the RGB phase is also dependent on the star's initial mass. For lower mass stars the RGB phase is more pronounced compared to higher mass stars. Hence the tip of the RGB (maximal radius of a star during the RGB phase) decreases with increasing mass. At the same time, because of the increase in mass, the dynamical tide dissipation also increases (see Eq. 13). This results in the dynamical tide dissipation becoming more important during the HB phase for higher mass stars. Because of these two effects, the dynamical tide dissipation is important for companions at larger orbital distances than the primary's radius reached at the tip of the RGB (see Fig. 11 and 12).

When increasing further in mass to the most massive model of $4 M_{\odot}$ (see Fig. 13), the convective envelope goes through a similar evolution when the star is contracting gradually after the start of helium burning. Hence the dissipation from both the equilibrium and dynamical tides increases, with similar relative strengths as for the $3.5 M_{\odot}$ model (Fig. 12). When the star is fully contracted throughout the HB, the convective envelope is smaller for the $4 M_{\odot}$ model, reducing both the equilibrium and dynamical tide dissipation during this phase, where the dynamical tide dissipation is affected the most, reducing its relative importance. This effect is similar to the shift of convective to radiative envelope during the MS for 1 to $1.4 M_{\odot}$ models.

During the AGB phase, the trends of the equilibrium and dynamical tidal dissipation remain similar for all masses. At the start of the AGB phase, the ratio of the dissipation of the dynamical to equilibrium tide starts to decrease due to the increase in the primary's radius, similar to the RGB phase. As the relative importance of the dynamical tide dissipation increases during the HB phase, the relative importance also increases at the start of the AGB phase, but its importance becomes negligible early in the AGB phase. In the late stages of the AGB phase, the star will undergo thermal pulses. This will alter the internal structure of the star, and therefore the tidal dissipation. During a thermal pulse the star will undergo helium shell flashes, temporarily increasing its stellar radius, to afterwards go back to its original state. Therefore the equilibrium tide dissipation will increase during such a pulse. The dynamical tide dissipation will change as well, but throughout all the models the dynamical tide dissipation is negligible compared to the equilibrium tide dissipation during these thermal pulses.

5. Conclusion

This study investigated the dissipation of the equilibrium and dynamical tides along the entire evolution of stars, with a strong focus on the evolved phases. A grid of stellar evolutionary models was created with initial mass between 1 and $4 M_{\odot}$. This allows the investigation of different stellar evolutionary effects on the tidal dissipation, such as the difference between a convective

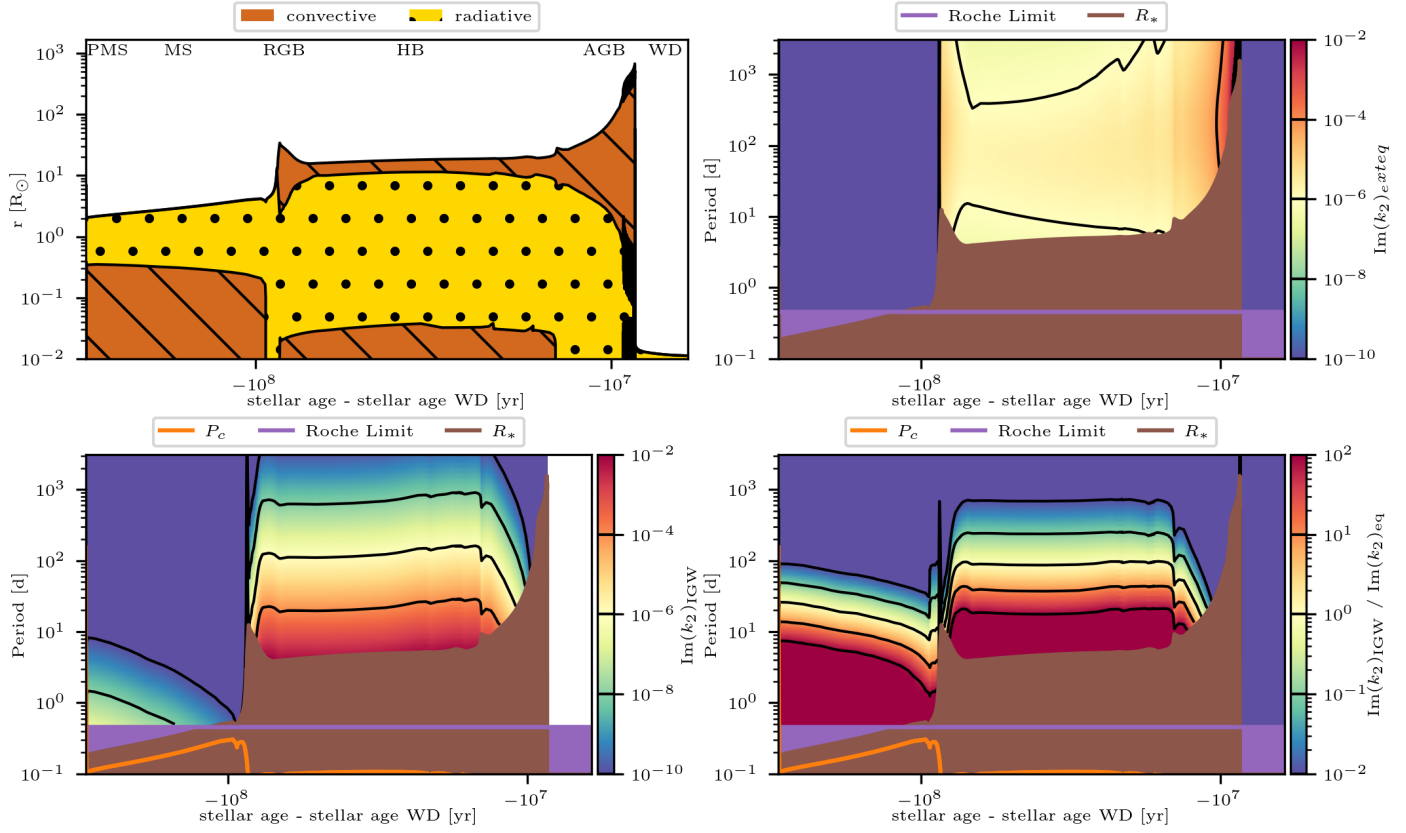


Fig. 12. Same as Fig. 11, but for a $M_{\text{ZAMS}} = 3.5 \text{ M}_{\odot}$ star.

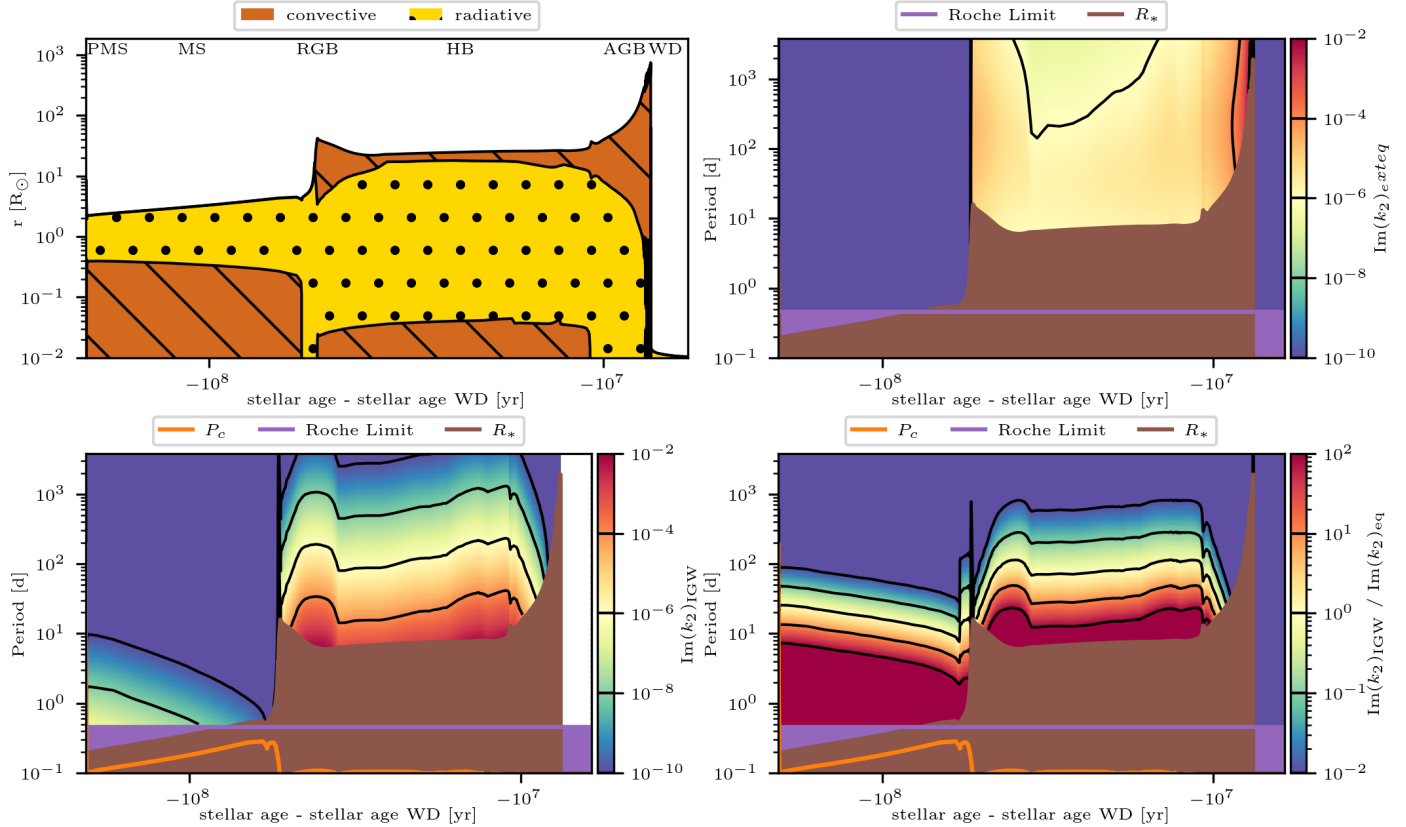


Fig. 13. Same as Fig. 11, but for a $M_{\text{ZAMS}} = 4 \text{ M}_{\odot}$ star.

or radiative envelope during the MS, or the difference between a helium flash or gradual helium burning. Using these models we investigated the dependence on the orbital period, the mass of the primary star, and the mass of the companion. For stars with a sufficiently low primary mass such that the star has a radiative core and a convective envelope in the MS, the dynamical tide dissipation is dominant for orbital periods shorter than a few days, in agreement with Terquem et al. 1998; Goodman & Dickson 1998; Barker & Ogilvie 2010; Ahuir et al. 2021a, while the equilibrium tide dissipation dominates for orbital periods longer than 100 days. For stars with a sufficiently high initial mass that the star has a radiative envelope and a convective core in the MS, tidal dissipation is dominated by the dynamical tide originating from the core for short orbital periods, in agreement with Zahn (1975). For longer orbital periods, the equilibrium tide dissipation dominates. During the RGB, the importance of the dynamical tide dissipation decreases as the radius of the star increases. At the start of the HB, the dynamical tide dissipation becomes more important again, as the radius of the star decreases either instantaneously in a helium flash or steadily when helium burning starts gradually. During the HB the importance of the dynamical tide dissipation increases with increasing stellar mass. For sufficiently high mass ($4 M_{\odot}$) the importance of the dynamical tide dissipation decreases instead of increasing as the size of the convective envelope shrinks. During the AGB, the equilibrium tide dissipation becomes dominant again due to the increase in stellar radius, similar to the RGB phase. During the WD phase, as the star is fully radiative, our formalism for the dynamical tide does not apply. However, this might be different when the dynamical tidal dissipation from standing g-modes and f-modes (Fuller & Lai 2011, 2012, 2013, 2014; Veras & Fuller 2019) are taken into account.

In a next step, these outcomes can be included in calculating the rate of change of the orbital distance of planetary and stellar companions along stellar evolution. The numerical model of a coplanar circular star-planet system called ESPEM (Benbakoura et al. 2019; Ahuir et al. 2021b) can be used to study the orbital evolution of a star-planet and star-star system. This model includes the tidal dissipation of the equilibrium tide dissipation as well as the dynamical tide arising from inertial waves propagating in convective envelopes. This code will be improved by including the dissipation of the dynamical tide arising from progressive internal gravity waves (similar to Lazovik 2021, 2023), necessary for systems containing an evolved star. Furthermore the rotation of the primary star is reduced due to magnetic breaking in ESPEM (Benbakoura et al. 2019; Ahuir et al. 2021b). In evolved stars the magnetic breaking becomes negligible compared to the torque arising from the strong mass loss during this phase, which is not included in ESPEM as of now. This can be included by introducing a mass losing outer shell (Madappatt et al. 2016), which depends on the current mass-loss rate of the star. The mass-loss rate of AGB stars can be dependent on the presence of a companion, but ongoing work is still determining how much (Decin et al. 2020; Aydi & Mohamed 2022). This will allow the study of the orbital distance evolution of star-planet and star-star systems around evolved stars and the resulting companion orbital distance and occurrence rate as this has been done for solar-like stars during the MS in García et al. (2023).

Furthermore, the orbital evolution of star-planet systems around evolved stars can be studied taking into account the last breakthrough obtained through asteroseismology. Asteroseismology is now revealing the presence of potentially strong magnetic fields in the core of red giants (Li et al. 2022, 2023; Deheuvels et al. 2023). Such strong magnetic fields can deeply

modify the propagation of mixed modes, which behave as gravity modes in the core of red giants (e.g. Fuller et al. 2015; Bugnet et al. 2021; Mathis et al. 2021; Li et al. 2022; Mathis & Bugnet 2023; Rui & Fuller 2023; Rui et al. 2024) and can be potentially excited by tides. The effect of such potential modification of the propagation and dissipation of such tidal modes still requires a dedicated investigation, potentially altering the dynamics of planetary systems around these magnetic stars.

Acknowledgements. The authors would like to thank Matthias Fabry, Hannah Brinkman, Timothy Van Reeth, and Pablo Marchant for their help and support in setting up the MESA stellar evolution models. The authors would also like to thank Clément Baruteau for the useful discussions. M. Esseldeurs and L. Decin acknowledge support from the FWO grants G099720N and G0B3823N, the KU Leuven C1 excellence grant MAESTRO C16/17/007 and the KU Leuven IDN grant ESCHER IDN/19/028. S. Mathis acknowledges support from the PLATO CNES grant at CEA/DAp, from the Programme National de Planétologie (PNP-CNRS/INSU) and from the European Research Council through HORIZON ERC SyG Grant 4D-STAR 101071505.

References

- Abramowitz, M. & Stegun, I. A. 1972, Handbook of Mathematical Functions
- Aerts, C., Christensen-Dalsgaard, J., & Kurtz, D. W. 2010, Asteroseismology
- Aerts, C., Mathis, S., & Rogers, T. M. 2019, ARA&A, 57, 35
- Auir, J., Mathis, S., & Amard, L. 2021a, A&A, 651, A3
- Auir, J., Strugarek, A., Brun, A. S., & Mathis, S. 2021b, A&A, 650, A126
- Alvan, L., Strugarek, A., Brun, A. S., Mathis, S., & Garcia, R. A. 2015, A&A, 581, A112
- Amard, L., Palacios, A., Charbonnel, C., Gallet, F., & Bouvier, J. 2016, A&A, 587, A105
- Asplund, M., Grevesse, N., Sauval, A. J., & Scott, P. 2009, ARA&A, 47, 481
- Auclair Desrotour, P., Mathis, S., & Le Poncin-Lafitte, C. 2015, A&A, 581, A118
- Aydi, E. & Mohamed, S. 2022, MNRAS, 513, 4405
- Barker, A. J. 2020, MNRAS, 498, 2270
- Barker, A. J. & Ogilvie, G. I. 2010, MNRAS, 404, 1849
- Beck, P. G., Grossmann, D. H., Steinwender, L., et al. 2023, arXiv e-prints, arXiv:2307.10812
- Beck, P. G., Mathis, S., Gallet, F., et al. 2018, MNRAS, 479, L123
- Beck, P. G., Mathur, S., Hambleton, K., et al. 2022, A&A, 667, A31
- Benbakoura, M., Réville, V., Brun, A. S., Le Poncin-Lafitte, C., & Mathis, S. 2019, A&A, 621, A124
- Blöcker, T. 1995, A&A, 297, 727
- Bolmont, E., Gallet, F., Mathis, S., et al. 2017, A&A, 604, A113
- Bolmont, E. & Mathis, S. 2016, Celestial Mechanics and Dynamical Astronomy, 126, 275
- Bugnet, L., Prat, V., Mathis, S., et al. 2021, A&A, 650, A53
- Ceillier, T., Tayar, J., Mathur, S., et al. 2017, A&A, 605, A111
- Cinquegrana, G. C. & Joyce, M. 2022, Research Notes of the American Astronomical Society, 6, 77
- Decin, L., Montargès, M., Richards, A. M. S., et al. 2020, Science, 369, 1497
- Deheuvels, S., Li, G., Ballot, J., & Lignières, F. 2023, A&A, 670, L16
- Dhouib, H., Baruteau, C., Mathis, S., et al. 2023, arXiv e-prints, arXiv:2311.03288
- Döllinger, M. P. & Hartmann, M. 2021, ApJS, 256, 10
- Duguid, C. D., Barker, A. J., & Jones, C. A. 2020, MNRAS, 497, 3400
- Fuller, J. 2017, MNRAS, 472, 1538
- Fuller, J., Cantiello, M., Stello, D., Garcia, R. A., & Bildsten, L. 2015, Science, 350, 423
- Fuller, J. & Lai, D. 2011, MNRAS, 412, 1331
- Fuller, J. & Lai, D. 2012, MNRAS, 421, 426
- Fuller, J. & Lai, D. 2013, MNRAS, 430, 274
- Fuller, J. & Lai, D. 2014, MNRAS, 444, 3488
- Gallet, F., Bolmont, E., Mathis, S., Charbonnel, C., & Amard, L. 2017, A&A, 604, A112
- García, R. A., Gourvès, C., Santos, A. R. G., et al. 2023, A&A, 679, L12
- García-Segura, G., Villaver, E., Manchado, A., Langer, N., & Yoon, S. C. 2016, ApJ, 823, 142
- Goldreich, P. & Nicholson, P. D. 1989, ApJ, 342, 1079
- Goodman, J. & Dickson, E. S. 1998, ApJ, 507, 938
- Heney, L., Vardya, M. S., & Bodenheimer, P. 1965, ApJ, 142, 841
- Hon, M., Huber, D., Rui, N. Z., et al. 2023, Nature, 618, 917
- Jermyn, A. S., Bauer, E. B., Schwab, J., et al. 2023, ApJS, 265, 15
- Kaula, W. M. 1962, AJ, 67, 300
- Kawaler, S. D. 1988, ApJ, 333, 236
- Lazovik, Y. A. 2021, MNRAS, 508, 3408

- Lazovik, Y. A. 2023, MNRAS, 520, 3749
- Lee, B.-C., Do, H.-J., Park, M.-G., et al. 2023, A&A, 678, A106
- Li, G., Deheuvels, S., Ballot, J., & Lignières, F. 2022, Nature, 610, 43
- Li, G., Deheuvels, S., Li, T., Ballot, J., & Lignières, F. 2023, A&A, 680, A26
- Love, A. E. H. 1911, Some Problems of Geodynamics
- Madappatt, N., De Marco, O., & Villaver, E. 2016, MNRAS, 463, 1040
- Marigo, P. & Aringer, B. 2009, A&A, 508, 1539
- Mathis, S. 2013, in Lecture Notes in Physics, Berlin Springer Verlag, ed. M. Goupil, K. Belkacem, C. Neiner, F. Lignières, & J. J. Green, Vol. 865, 23
- Mathis, S. 2015, A&A, 580, L3
- Mathis, S. 2018, in Handbook of Exoplanets, ed. H. J. Deeg & J. A. Belmonte, 24
- Mathis, S. & Bugnet, L. 2023, A&A, 676, L9
- Mathis, S., Bugnet, L., Prat, V., et al. 2021, A&A, 647, A122
- Mathis, S. & Le Poncin-Lafitte, C. 2009, A&A, 497, 889
- McDonald, I. & Zijlstra, A. A. 2015, MNRAS, 448, 502
- Mustill, A. J. & Villaver, E. 2012, ApJ, 761, 121
- Nowak, G., Niedzielski, A., Wolszczan, A., Adamów, M., & Maciejewski, G. 2013, ApJ, 770, 53
- Ogilvie, G. I. 2013, MNRAS, 429, 613
- Ogilvie, G. I. 2014, ARA&A, 52, 171
- Ogilvie, G. I. & Lin, D. N. C. 2004, ApJ, 610, 477
- Ogilvie, G. I. & Lin, D. N. C. 2007, ApJ, 661, 1180
- Oomen, G.-M., Van Winckel, H., Pols, O., et al. 2018, A&A, 620, A85
- Paxton, B., Bildsten, L., Dotter, A., et al. 2011, ApJS, 192, 3
- Paxton, B., Cantiello, M., Arras, P., et al. 2013, ApJS, 208, 4
- Paxton, B., Marchant, P., Schwab, J., et al. 2015, ApJS, 220, 15
- Paxton, B., Schwab, J., Bauer, E. B., et al. 2018, ApJS, 234, 34
- Paxton, B., Smolec, R., Schwab, J., et al. 2019, ApJS, 243, 10
- Pereira, F., Grunblatt, S. K., Psaridi, A., et al. 2024, MNRAS, 527, 6332
- Reimers, D. 1975, in Problems in stellar atmospheres and envelopes., 229–256
- Remus, F., Mathis, S., & Zahn, J. P. 2012, A&A, 544, A132
- Rieutord, M. 2015, Fluid Dynamics: An Introduction
- Rui, N. Z. & Fuller, J. 2023, MNRAS, 523, 582
- Rui, N. Z., Ong, J. M. J., & Mathis, S. 2024, MNRAS, 527, 6346
- Sato, B., Izumiura, H., Toyota, E., et al. 2008, PASJ, 60, 539
- Saunders, N., Grunblatt, S. K., Huber, D., et al. 2022, AJ, 163, 53
- Siess, L., Dufour, E., & Forestini, M. 2000, A&A, 358, 593
- Skumanich, A. 1972, ApJ, 171, 565
- Terquem, C., Papaloizou, J. C. B., Nelson, R. P., & Lin, D. N. C. 1998, ApJ, 502, 788
- Van Winckel, H. 2003, ARA&A, 41, 391
- Veras, D. & Fuller, J. 2019, MNRAS, 489, 2941
- Verbunt, F. & Phinney, E. S. 1995, A&A, 296, 709
- Viallet, M., Meakin, C., Prat, V., & Arnett, D. 2015, A&A, 580, A61
- Vlemmings, W. H. T., Khouri, T., De Beck, E., et al. 2018, A&A, 613, L4
- Weinberg, N. N., Sun, M., Arras, P., & Essick, R. 2017, ApJ, 849, L11
- Witte, M. G. & Savonije, G. J. 2002, A&A, 386, 222
- Wu, Y. 2005a, ApJ, 635, 674
- Wu, Y. 2005b, ApJ, 635, 688
- Zahn, J. P. 1966, Annales d'Astrophysique, 29, 313
- Zahn, J. P. 1975, A&A, 41, 329
- Zahn, J. P. 1977, A&A, 57, 383
- Zahn, J. P. 1989, A&A, 220, 112
- Zahn, J. P. 1992, A&A, 265, 115
- Zahn, J. P. & Bouchet, L. 1989, A&A, 223, 112

Appendix A: Comparison to (Ahuir et al. 2021a)

To benchmark our implementation of the tidal dissipation prescriptions, as well as to estimate the robustness of the solutions for different stellar evolutionary codes, we compare our results to the results obtained by Ahuir et al. (2021a) who used stellar models with initial masses between 0.4 and 1.4 M_{\odot} using the stellar evolution code STAREVOL (Siess et al. 2000; Amard et al. 2016). In Fig. A.1 on the top, the equilibrium and dynamical tide are shown as calculated by Ahuir et al. (2021a) in blue, orange and green for a 1, 1.2 and 1.4 M_{\odot} star respectively. They calculate the equilibrium tide dissipation assuming a thin convective envelope, such that the equilibrium tide dissipation becomes:

$$\text{Im}(k_2)_{\text{eq}} = \frac{696}{35} |t_c \omega_t| \frac{R_{\star}}{GM_1} V_c^2 (1 - \beta) \frac{1 - \alpha^9}{1 - \alpha^3} F(\omega_t), \quad (\text{A.1})$$

where V_c is the convective velocity, α and β are the ratio of the convective to the total radius and mass respectively, and $F(\omega_t)$ is the dependence of the turbulent viscosity on the tidal frequency (see Eq. 12). Evolved systems have a huge convective envelope, therefore this study calculates the equilibrium tide dissipation for the full star (see Sect. 2.3.1). On the bottom of Fig. A.1, the equilibrium tide dissipation is shown both using the formulation of Ahuir et al. (2021a) and this study (Sect. 2.3.1), as well as the dynamical tidal dissipation computed for the MESA models used in this study. The results are computed for a Jupiter mass planet at an orbit of a day, until the planet would be inside the star. The results are in good agreement (and thus in agreement with those of Terquem et al. 1998; Goodman & Dickson 1998; Barker & Ogilvie 2010). Looking at the 1 and 1.2 M_{\odot} stars, the two results always lie in the same order of magnitude for both the equilibrium (looking at the calculation using Eq. A.1) and dynamical tide dissipation, where the only difference is the lifetime of the star. For the 1.4 M_{\odot} star, the results are slightly different. During the PMS and sub-giant phase the results are the same, but during the MS both the equilibrium and dynamical tide dissipation are weaker in this study. This is because the star has a negligible convective envelope during the MS, and as the stellar evolution codes use different opacity tables, these regions are slightly different when using MESA or STAREVOL, resulting in different results. However, although the relative difference is large, the tidal dissipation is small in both cases. This validates our implementation in MESA and show that the results are robust for different stellar structure and evolution codes. Looking at the different method of calculating the equilibrium tide dissipation, this makes a difference throughout the entire evolution of the star. As more approximations were made to estimate the equilibrium tide dissipation in Ahuir et al. (2021a), therefore the dissipation of the equilibrium tide calculated in this study is more reliable.

Appendix B: Tidal dissipation evaluation for complementary masses of the stellar evolution grid.

This section contains the tidal dissipation figures for the remaining stellar evolutionary models not illustrated in the main text. Their main patterns have been identified and explained in Sect. 4.5.

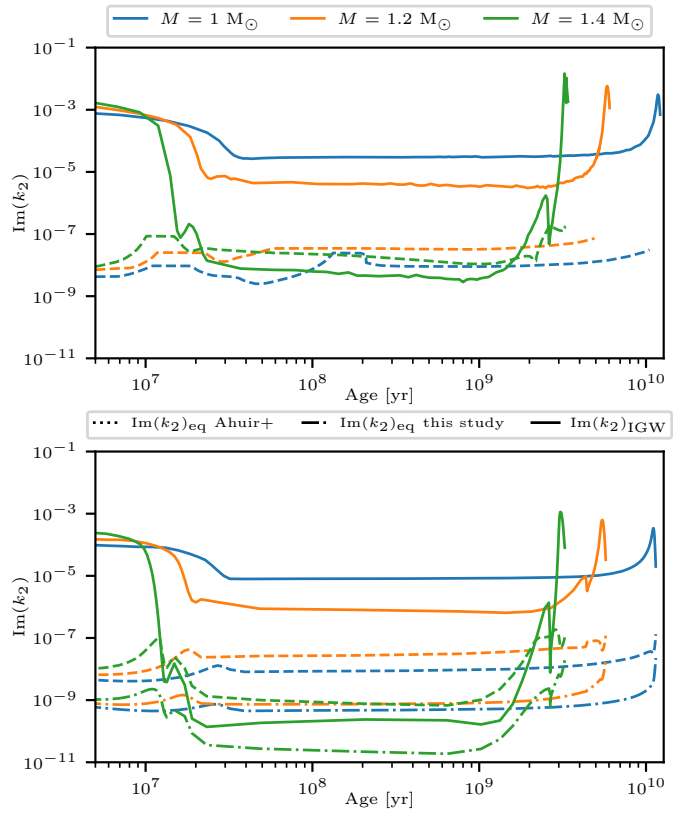


Fig. A.1. Complex part of the Love number for equilibrium ($\text{Im}(k_2)_{\text{eq}}$) and dynamical ($\text{Im}(k_2)_{\text{IGW}}$) tides, as a function of stellar age, for both Ahuir et al. (2021a) in the upper plot and this study in the lower plot.

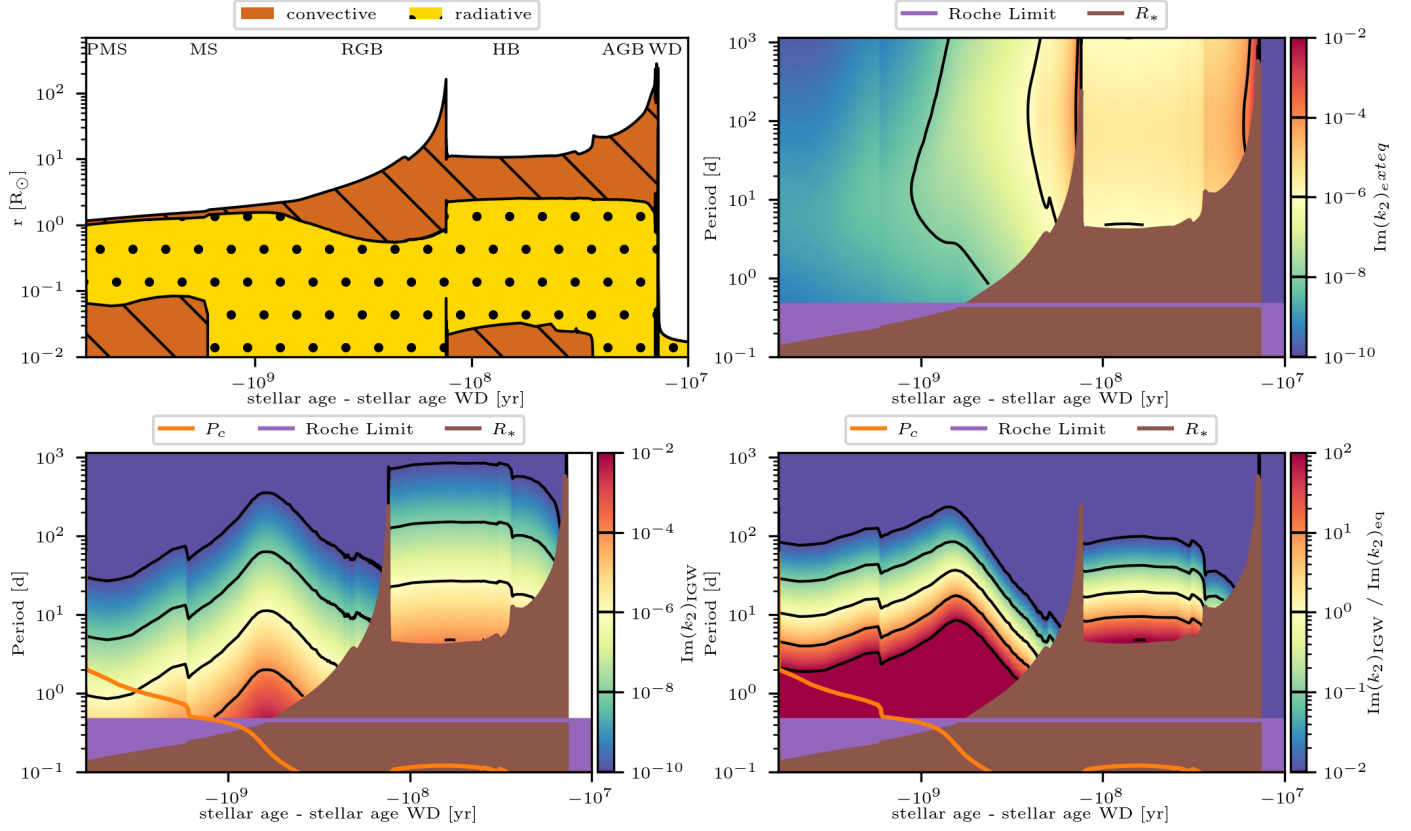


Fig. B.1. Same as Fig. 11, but for a $M_{\text{ZAMS}} = 1.2 \text{ M}_{\odot}$ star.

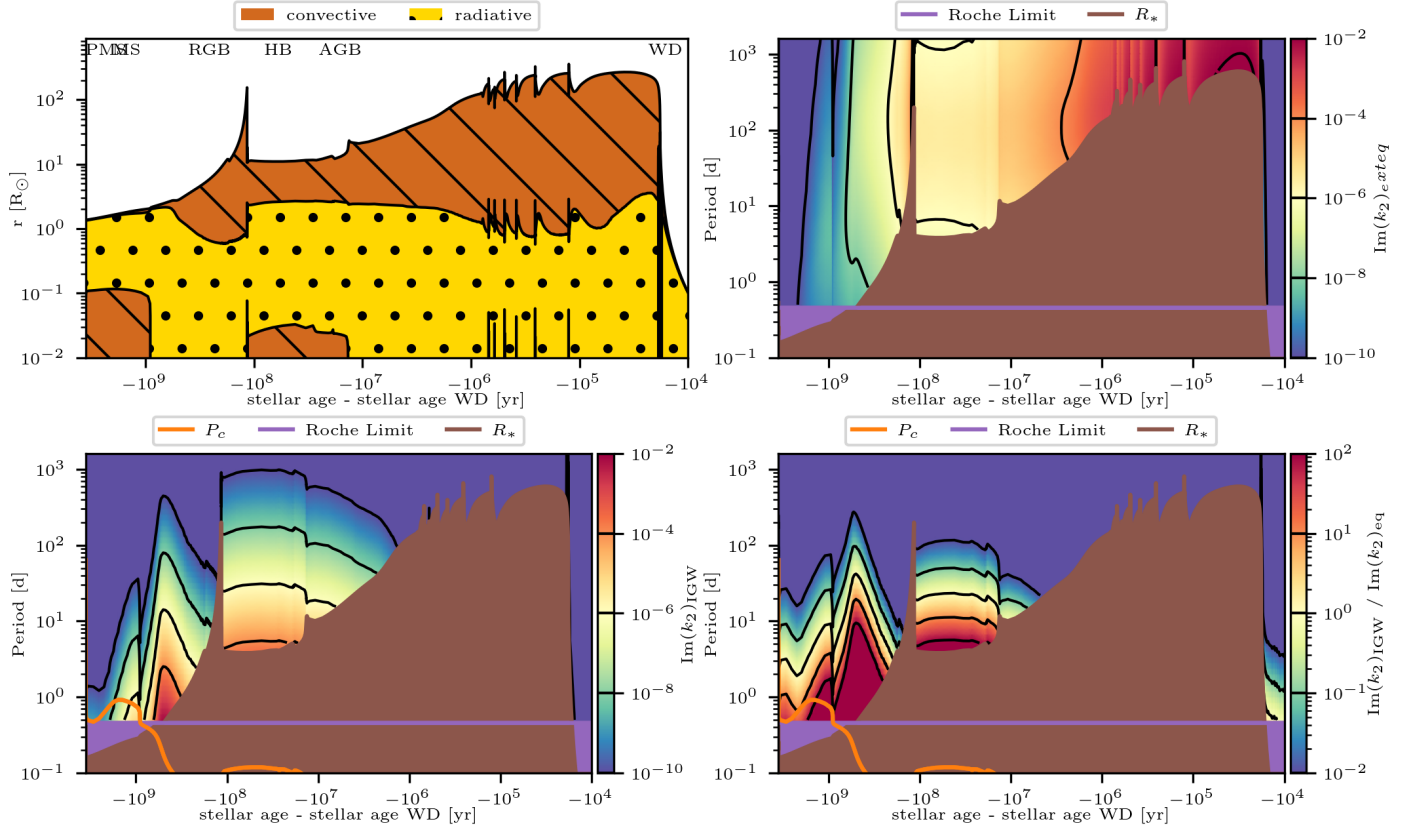


Fig. B.2. Same as Fig. 11, but for a $M_{\text{ZAMS}} = 1.4 \text{ M}_{\odot}$ star.

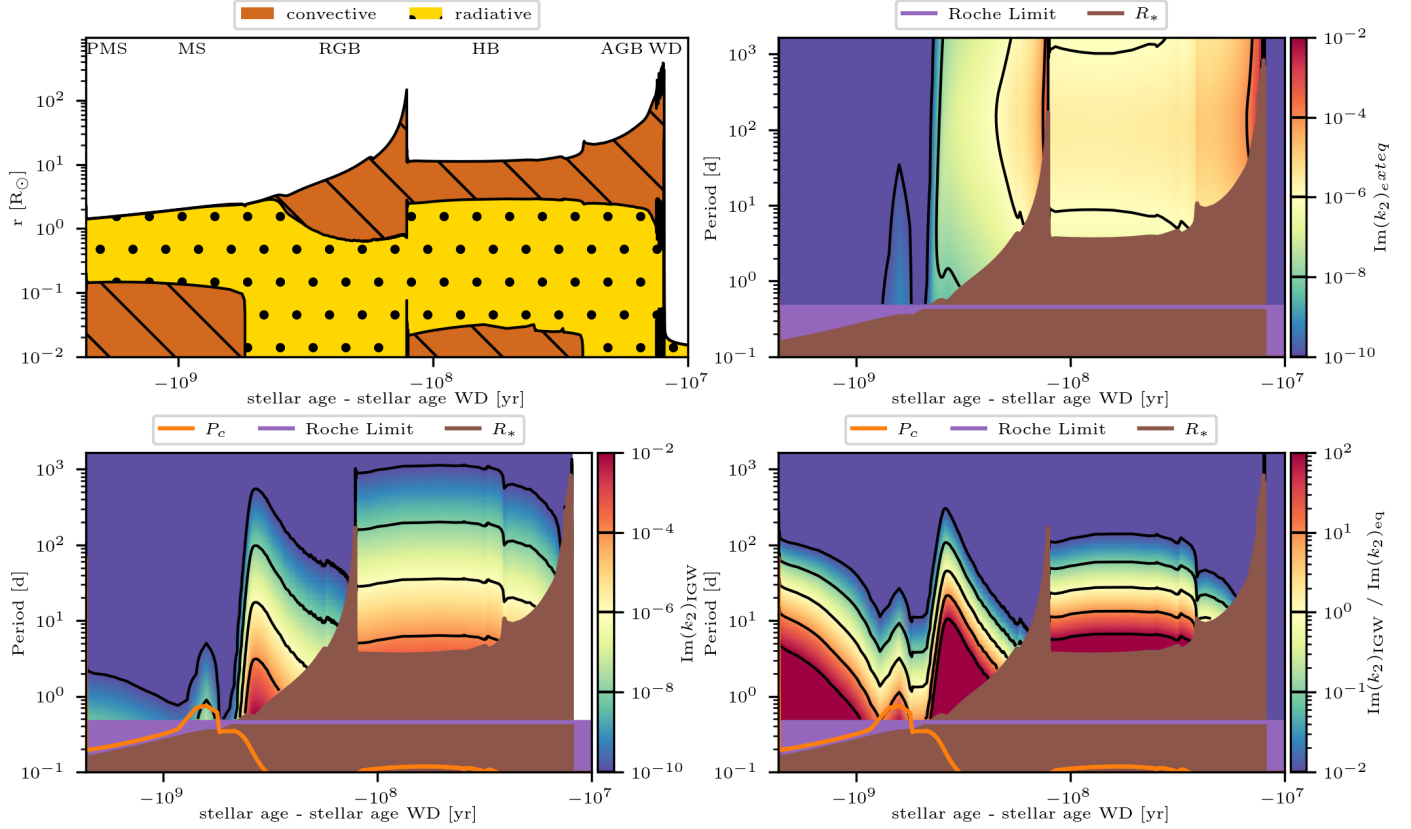


Fig. B.3. Same as Fig. 11, but for a $M_{\text{ZAMS}} = 1.6 \text{ M}_\odot$ star.

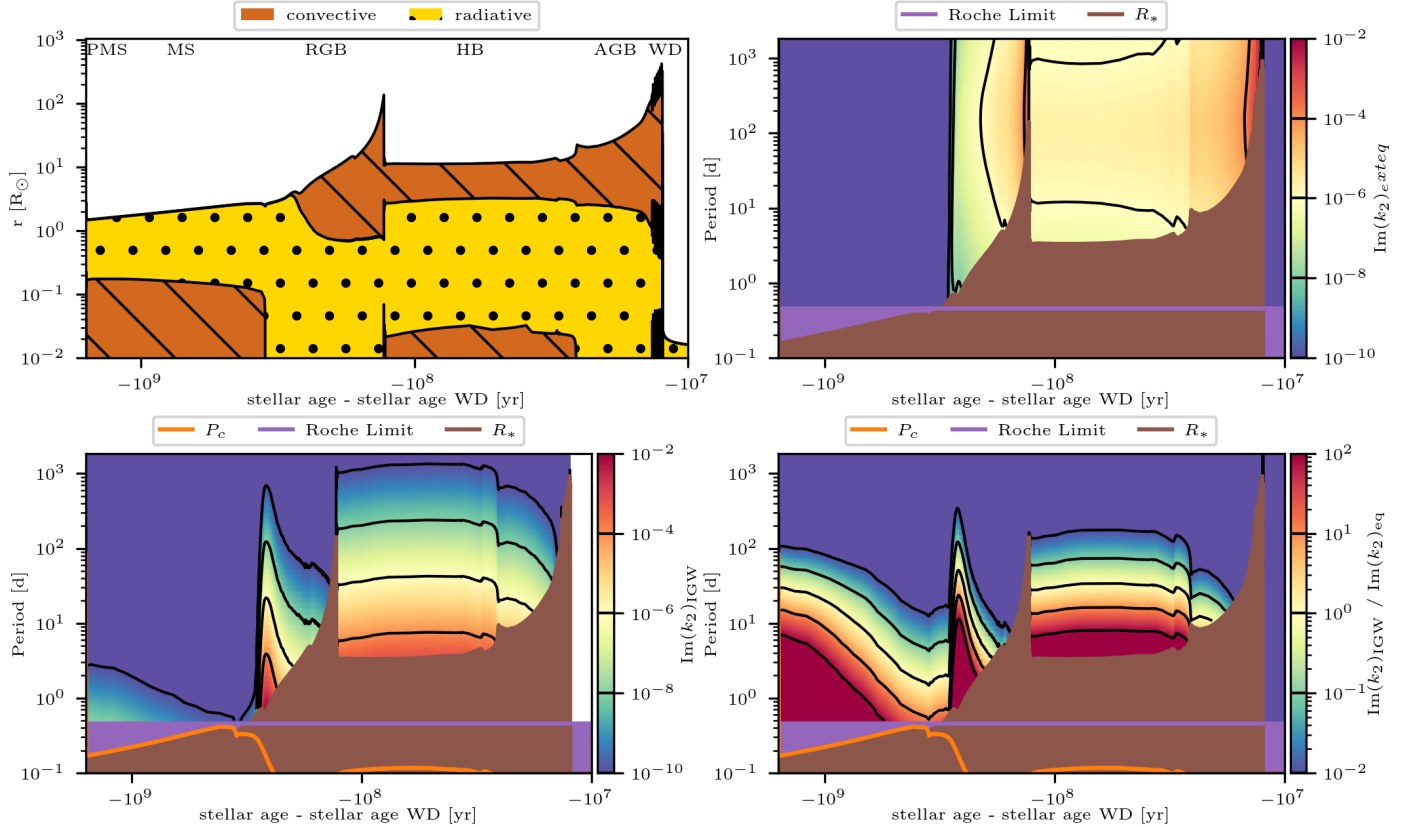


Fig. B.4. Same as Fig. 11, but for a $M_{\text{ZAMS}} = 1.8 \text{ M}_\odot$ star.

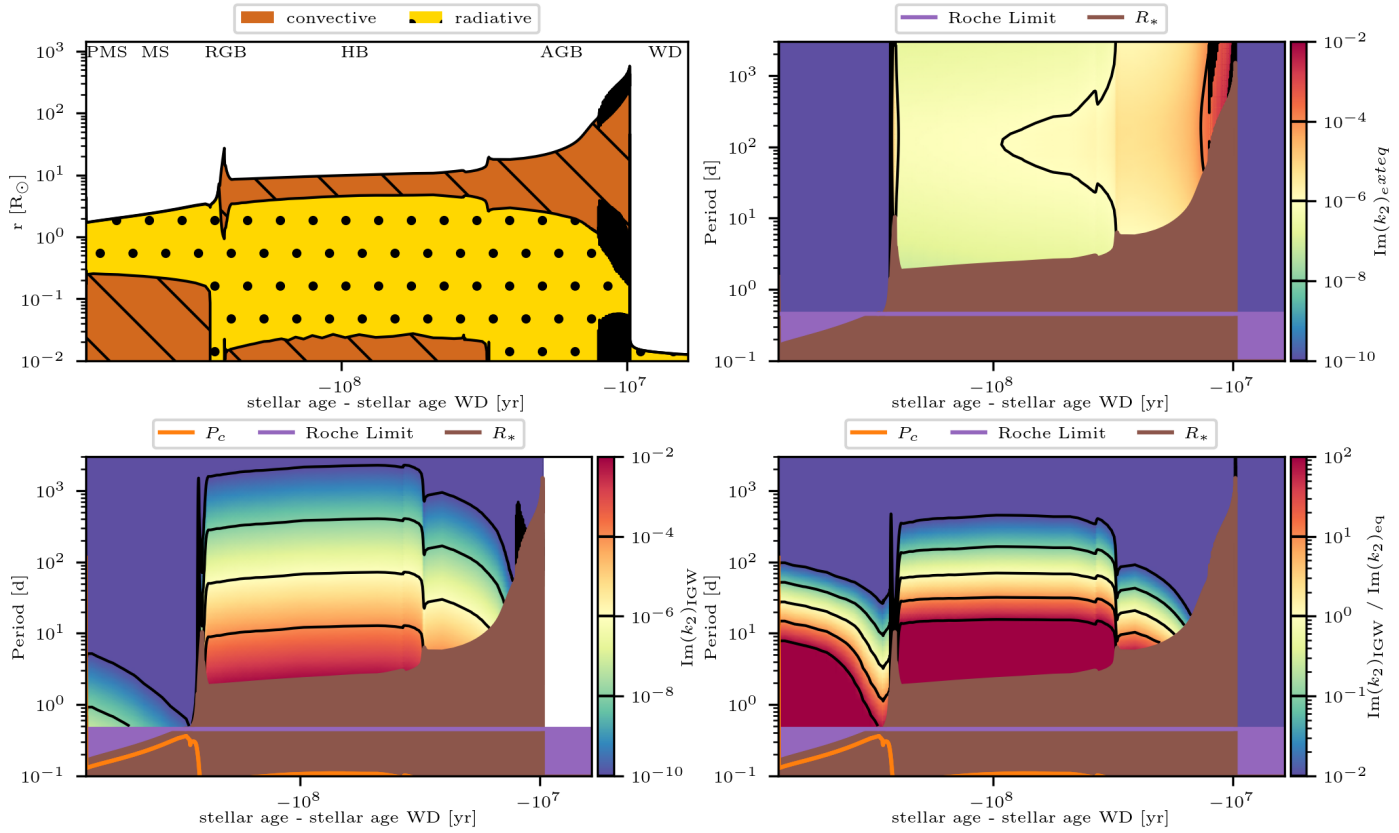


Fig. B.5. Same as Fig. 11, but for a $M_{\text{ZAMS}} = 2.5 \text{ M}_{\odot}$ star.

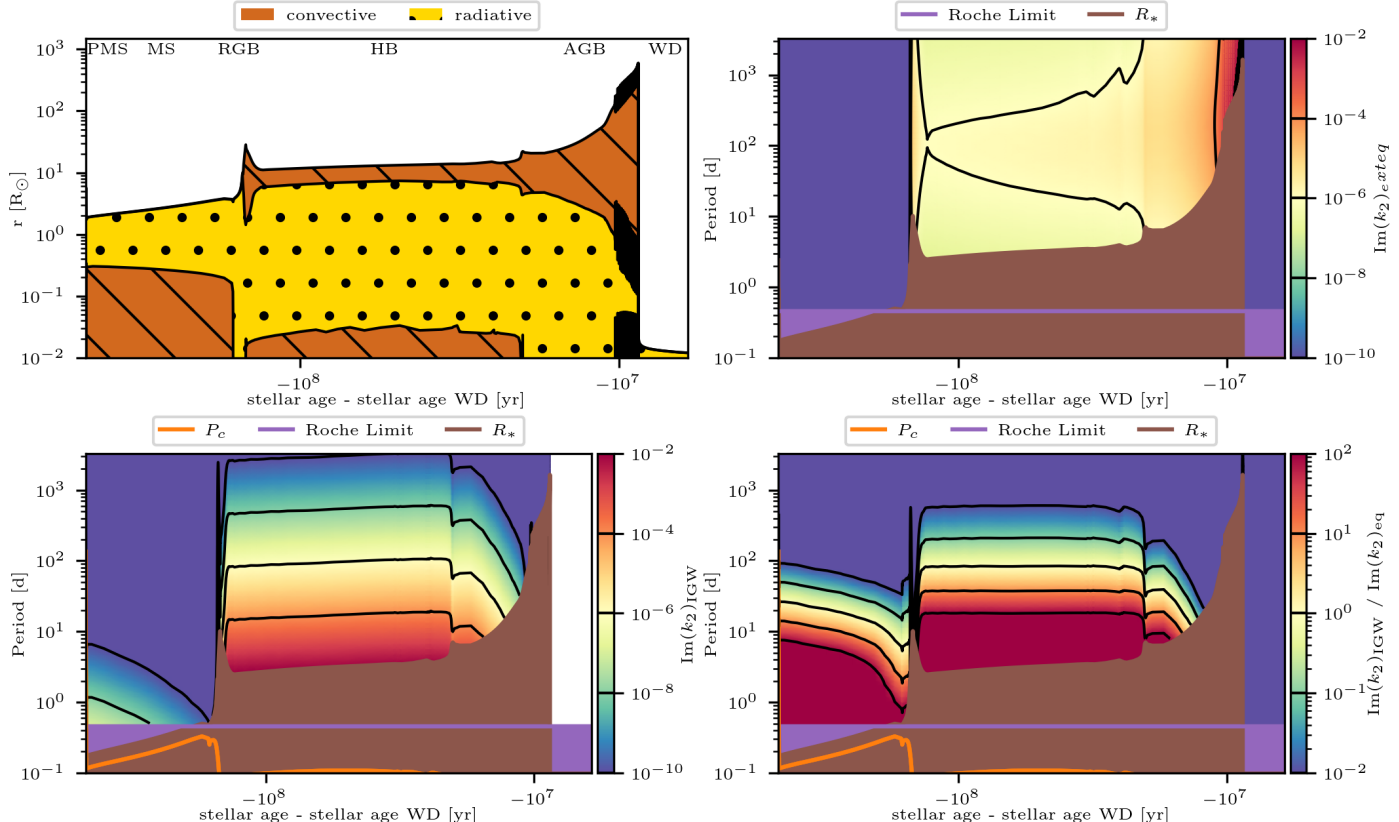


Fig. B.6. Same as Fig. 11, but for a $M_{\text{ZAMS}} = 3 \text{ M}_{\odot}$ star.

Appendix C: MESA inlist

The MESA (release-r23.05.1) inlist we use in this study is reported hereafter. Here “initial_mass = mass” refers to the initial mass of the star and “Blocker_scaling_factor = Blocker” to the Blöcker scaling factor for AGB mass-loss; $\eta_{\text{blöcker}} = 0.05$ for masses below $2 M_{\odot}$ and $\eta_{\text{blöcker}} = 0.1$ for masses above $2 M_{\odot}$.

&star_job

```
create_pre_main_sequence_model = .true.

! network
auto_extend_net = .true.
h_he_net = 'basic.net'
co_net = 'co_burn.net'
adv_net = 'approx21.net'

! opacities
initial_zfracs = 6 ! for L03 solar scaling

/ !end of star_job namelist
```

&kap

Zbase = 0.0134d0

```
use_Type2_opacities = .true.
kap_file_prefix = 'a09'
kap_C0_prefix = 'a09_co'
kap_lowT_prefix = 'AESOPUS'
AESOPUS_filename = 'AESOPUS_AGSS09.h5'
```

/ ! end of kap namelist

&controls

log_L_lower_limit = -1

```
varcontrol_target = 1d-4
min_timestep_limit = 1d-10
```

```
initial_mass = Mass
initial_z = 0.0134d0
```

```
mixing_length_alpha = 1.931
MLT_option = 'Henyey'
```

```
atm_option = 'T_tau'
atm_T_tau_relation = 'Eddington'
atm_T_tau_opacity = 'fixed'
```

```
cool_wind_RGB_scheme = 'Reimers'
cool_wind_AGB_scheme = 'Blocker'
RGB_to_AGB_wind_switch = 1d-4
Reimers_scaling_factor = 0.477d0
Blocker_scaling_factor = Blocker
```

```
set_min_D_mix = .true.
min_D_mix = 1d1
```

```
num_cells_for_smooth_gradL_composition_term = 10
threshold_for_smooth_gradL_composition_term = 0.02
num_cells_for_smooth_brunt_B = 10
```

threshold_for_smooth_brunt_B = 0.1

```
! relax tolerances for equations
report_solver_progress = .true.
use_gold_tolerances = .false.
```

```
solver_iters_timestep_limit = 20
solver_max_tries_before_reject = 30
```

```
energy_eqn_option = 'dedit'
convergence_ignore_equl_residuals = .true.
corr_coeff_limit = 1d-1
max_abs_rel_run_E_err = 1d-1
warn_when_large_rel_run_E_err = 1d-3
ignore_too_large_correction = .true.
scale_max_correction = 1d-2
ignore_min_corr_coeff_for_scale_max_correction = .true.
ignore_species_in_max_correction = .true.
use_superad_reduction = .true.
```

```
log_directory = 'LOGS'
photo_interval = 10
max_num_profile_models = 100000
profile_interval = 10
history_interval = 1
terminal_interval = 1
write_header_frequency = 1
```

/ ! end of controls namelist